Tribological Analysis of a Hermetic Reciprocating Compressor

by

AAMIR SHAHZAD

A Dissertation Submitted to the Graduate School of Sciences and Engineering in Partial Fulfillment of the Requirements for
the Degree of Doctor of Philosophy

in

Mechanical Engineering

KOÇ ÜNİVERSİTESİ

Date: January 05, 2024

Tribological studies of a hermetic reciprocating compressor piston

Koç University

Graduate School of Sciences and Engineering

This is to certify that I have examined this copy of a doctoral dissertation by

AAMIR SHAHZAD

and have found that it is complete and satisfactory in all respects, and that any and all revisions required by the final examining committee have been made.

Committee Members:

PROF. DR. İSMAIL LAZOĞLU (Advisor)

PROF. DR. DEMIRCAN CANADINC

PROF. DR. ALPER UZUN

PROF. DR. IBRAHIM ETEM SAKLAKOGLU

ASSIST. PROF. DR. ARMIN TURKSOY

Date: January 05, 2024

Dedicated to my family

ABSTRACT

A hermetic reciprocating compressor is one of the most critical parts for the energy efficiency of a household refrigerator. The tribological performance of the compressor's piston-cylinder pair could be enhanced through introducing micro-texture on the compressor's piston surface. In this thesis, an experimental study is presented to tribologically assess the effect of the micro-textured piston on the performance of the hermetically sealed reciprocating compressor. Effects of the micro-dimples texture of the piston on the compressor's coefficient of performance was investigated. Refrigerant leakage from the piston-cylinder clearance was decreased by 35% and the compressor's cooling capacity was observed to be increased slightly.

In addition, this thesis also presents a novel solution to the lubrication problem of an inverter-type hermetic reciprocating compressor used in household refrigerators during a low-speed (less than 2000 rpm) operation. The lubrication system is primarily based on an additively manufactured unibody pump.

Moreover, the thesis also aims to discuss the development of a cermet material for the manufacturing of piston via a multi-material negative additive manufacturing approach. The suggested methodology entails the layer-by-layer 3D printing of a negative mold geometry. The cermet slurry is cast into the mold gradually as it is built up layer-by-layer simultaneously. The cermet green body is then demolded by dispersing the mold in an organic solvent such as DCM. The multi-material 3D printing approach eliminated the shape retention problem of the slurry-based additive manufacturing system. A piston produced from cermet material through this method is found to be 10 times lighter than a conventional piston.

ÖZETÇE

Hermetik pistonlu kompresör, ev tipi bir buzdolabının enerji verimliliği için en kritik parçalardan biridir. Piston-silindir çiftinin tribolojik performansı, piston yüzeyinde mikro dokulama uygulanarak geliştirilebilir. Bu tezde, mikro dokulu pistonun sızdırmazlık dikkate alınarak kompresörün performansı üzerindeki etkisini tribolojik olarak değerlendirmek için deneysel bir çalışma sunulmaktadır. Pistonun mikro çukur dokusunun kompresörün performans katsayısı üzerindeki etkileri araştırıldı. Piston-silindir boşluğundan soğutucu akışkan sızıntısı %35 oranında azaldı ve kompresörün soğutma kapasitesinin bir miktar arttığı gözlemlendi.Ayrıca bu tez, ev tipi buzdolaplarında düşük hızlı (2000 rpm'den az) çalışma sırasında kullanılan invertör tipi hermetik pistonlu kompresörün yağlama yağı besleme sistemine yeni bir çözüm sunmaktadır. Sistem, eklemeli olarak üretilmiş yekpare bir pompaya dayanmaktadır.

Ayrıca tez, çok malzemeli negatif eklemeli imalat yaklaşımıyla piston üretimi için bir sermet malzemesinin geliştirilmesini tartışmayı amaçlamaktadır. Önerilen metodoloji, negatif bir kalıp geometrisinin katman katman 3D baskısını gerektirir. Sermet bulamacı, eş zamanlı olarak katman katman oluşturulduğu için kademeli olarak kalıba dökülür. Daha sonra sermet yeşil gövde, kalıbın DCM gibi bir organik çözücü içinde dağıtılmasıyla kalıptan çıkarılır. Çok malzemeli 3D baskı yaklaşımı, bulamaç bazlı eklemeli üretim sisteminin şekil tutma problemini ortadan kaldırdı. Bu yöntemle sermet malzemeden üretilen bir pistonun, geleneksel bir pistondan 10 kat daha hafif olduğu tespit edilmiştir.

ACKNOWLEDGEMENTS

Prof. Dr. Ismail Lazoglu is a kind supervisor who will challenge you enormously, however, he will always be there to help and guide you if you stumble and need support. It has been a true delight working on my Ph.D. thesis under his supervision. I am thankful to him for providing me with the opportunity to do research in a top-notch research environment at the Manufacturing and Automation Research Center (MARC). The thesis would not have been achievable without his advice, support, and encouragement. I would like to express my heartfelt gratitude to TUBITAK (The Scientific and Technological Research Council of Turkey) for their generous financial support, which made my Ph.D. studies possible. I also wish to thank members of Arcelik Compressor and R&D plants for their support and encouragement.

Koç University Surface Science and Technology Center (KUYTAM) has been an integral part of my Ph.D. studies. I would like to thank Dr. Hadi and Dr. Yagiz for their help and cooperation.

Koç University Boron and Advanced Materials Application and Research center (KUBAM), has also played a vital role during this journey. I offer my sincere gratitude to Prof. Dr. Ozge Balci and Aybike Paksoy.

I also thank my research collaborators for their support. I am extremely grateful to my fellow MARC members for their friendship and support throughout my doctoral studies. I would especially thank Dr. Shehreyar Ata Khan and Pouya Pashak for their valuable feedback and support.

Last but not least, I would like to thank my mother, brothers, and sisters back in Pakistan, who have always backed and believed in me. I am grateful to my wife, Sheeba, and kids, Afaq and Mah Roosh for their patience and unconditional love and support.

TABLE OF CONTENTS

LIST OF FIGURES

Nomenclature and Abbreviations

Roman symbols

d_h: Hydraulic diameter (m)

dt: time step size (s)

F: Force/load (N)

$\dot{m}$: mass flow rate (kg s^{-1})

N: rotational speed (rpm)

P: Power (W)

Q_c: Cooling capacity (W)

Re: Reynolds number

T: Temperature (°C)

t: time (s)

v: Kinematic viscosity (mm^2 s^{-1})

Greek symbols

ρ: Density (kg m^{-3})

μ: dynamic viscosity (Pa s)

Abbreviations

rpm: Revolution per minute

HV: Vicker hardness number

COP: Coefficient of performance

LST: Laser surface texture

CAD: Computer Aided Design

CFD: Computational Fluid Dynamics

DIW: Direct Ink Writing

FFF: Fused Filament Fabrication

MAPE: Mean absolute percentage error

MRF: Multi Reference Frame

PISO: Pressure-Implicit with Splitting of Operators

PLA: Polylactic acid

VoF: Volume of Fluid

Chapter 1

INTRODUCTION

1.1 Hermetic Reciprocating Compressor

The basic function of any compressor is increasing the working fluid pressure by reducing its specific volume. Compressors are used in many industries i.e., refrigeration, chemical, and power plants, etc. There are various types of compressors for a particular application field such as reciprocating, screw, and scroll compressors. For household refrigeration, hermetic reciprocating compressors are broadly employed for many decades.

Hermetic reciprocating compressors compress the refrigerant by decreasing the volume inside a cylinder by the reciprocating motion of a piston. The oscillatory movement of the piston is caused by the rotational motion of a crankshaft which is powered by an electric motor placed inside the shell of the compressor. The capacity of compressing the refrigerant with as little power as possible is known as coefficient of performance (COP) of the compressor. Hermetic reciprocating compressors are mainly of two types. The fixed-speed compressors are driven by a single-phase asynchronous motor and the inverter-type compressor is run by a direct current motor. The crankshaft of a hermetic reciprocating compressor performs an essential role in the lubrication system of the compressor. In a hermetic domestic refrigerating compressor, the lubrication oil is commonly provided by an integrated pumping system on the crankshaft which mainly comprises of a centrifugal pump and helical channels on the crankshaft. The centrifugal pump is partially immersed into the lubrication oil sump at the bottom of the shell and when the crankshaft rotates, the oil in the sump is pumped into the centrifugal pump and transported to the crankshaft helical channel. This process provides lubrication to all moving parts and hydrodynamic bearings of the hermetic reciprocating compressor. Fig. 1.1 illustrates the CAD model of the compressor used for the present study.

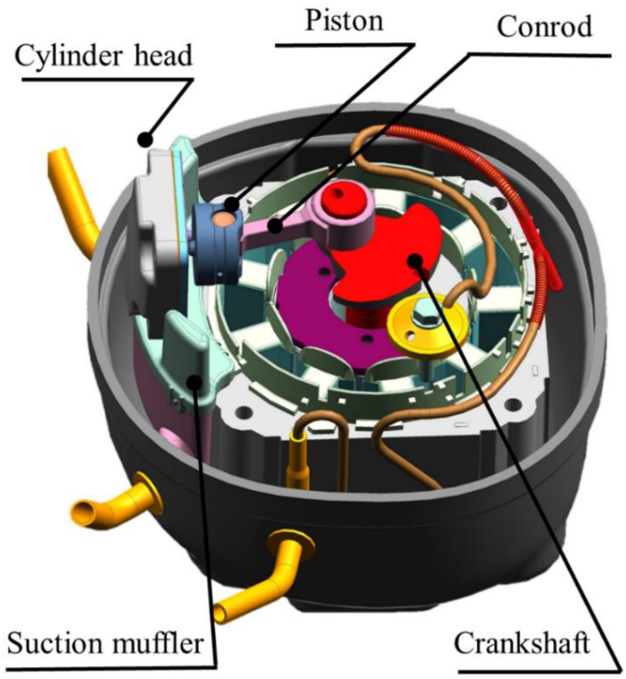

Figure 1.1CAD of Compressor

All the hermetic reciprocating compressor components are unified into a airtight steel casing and the connection to the refrigerator is made by connecting the suction and discharge tubes to the evaporator and condenser.

1.2 Lubrication of piston

In a refrigerator compressor, the small gap between the cylinder and piston is kept small (less than 10 microns) to prevent refrigerant leakage. This clearance plays a rather important role when it comes to lubrication as the piston starts moving in mixed or boundary lubrication conditions. Due to asperity contacts, lubrication oil flow is prevented which leads to oil pressure drop and a decrease in load carrying ability of the bearing. Minimizing frictional, power, and leakage losses while enhancing the life expectancy of the piston is the most important parameter when designing the piston.

Generally, a groove or channel is created on the piston surface to decrease the contact area and thus frictional losses.

1.3 Calorimetry test

Calorimeter test is used to measure the COP of the compressors at a steady-state condition. A sketch of a calorimeter test operations can be seen in Fig. 1.2.

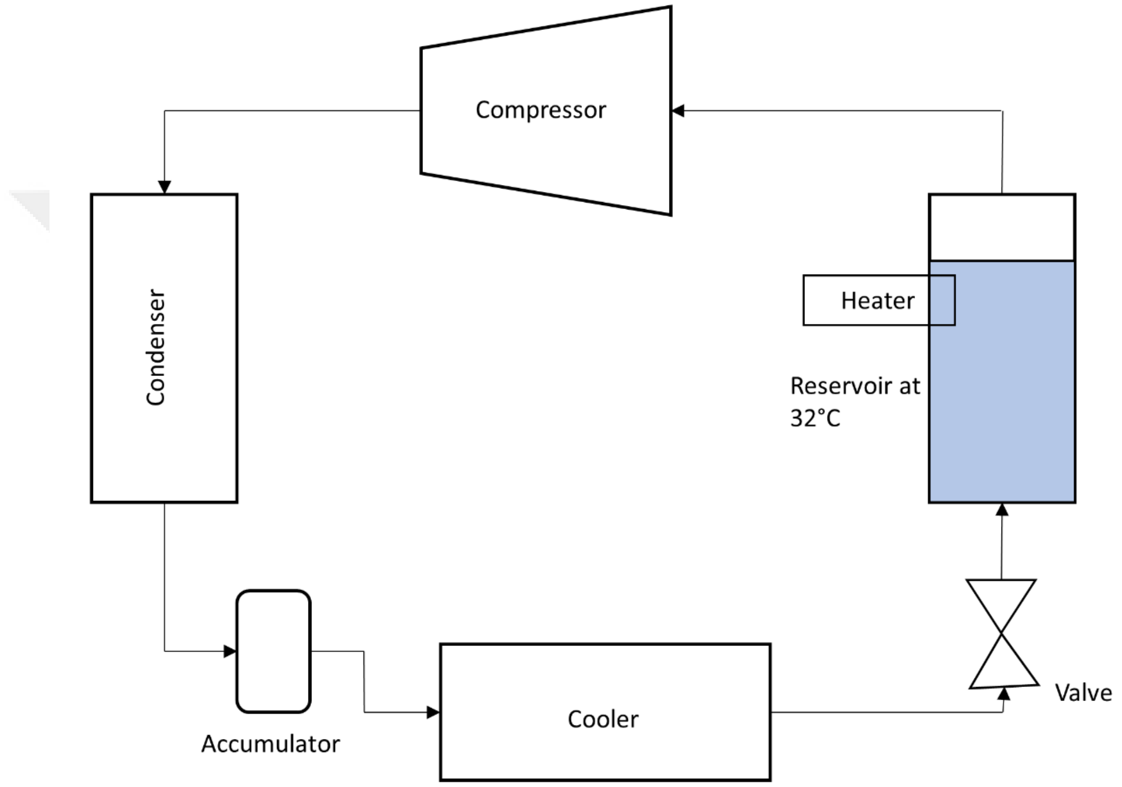

Figure 1.2 Schematic of Calorimeter

Starting from the compressor, the compressed refrigerant goes into the condenser where dissipation of heat occurs. The liquid refrigerant then enters an accumulator, from the accumulator it goes to the cooler where it is cooled down to room temperature. An expansion valve is then used to expand the refrigerant and to decrease the pressure and temperature. The refrigerant then enters a reservoir which contains a second gas at room temperature but at two phase condition. An electric heater is used to maintain the 32°C temperature in the reservoir. The pressure and temperature of the this second refrigerant drop due to the heat transfer between the two refrigerants. A wattmeter is used to measure the input power of the compressor.

To calculate the efficiency of the compressor the coefficient of performance can be measured by equation 1.1.

$$COP = \frac{\dot{Q}_0}{P} \tag{1.1}$$

Generally, for a household refrigerator, the COP of the compressor is investigated at ASHRAE conditions.

1.4 Coefficient of performance

The COP of the compressor could be increased either by increasing the cooling capacity of the compressor or by reducing the electrical power input. One way to increase the cooling capacity is to reduce the refrigerant leakage through the gap between piston and cylinder by having a continuous layer of lubrication oil at all working speeds. This could be achieved either by introducing micro-texturing on the piston surface which would act like a lubrication oil reservoir or by designing an efficient pump that could provide lubrication oil to all parts of the hermetic reciprocating compressor, especially the piston and cylinder pair. To reduce the electrical power input, reducing the mass of the piston could be an efficient solution. This could be accomplished by changing the material of the piston from conventional ferrous materials to composite and cermet materials.

1.5 Research aim

Cooling appliances such as refrigerators are an essential part of human life in the modern world. The hermetic reciprocating compressor is an integral and vital part of the refrigerator for energy efficiency. Increasing the performance coefficient of a hermetically sealed reciprocating compressor is the most critical challenge for the refrigerator manufacturing industry due to new energy regulations around the globe. Therefore, research should be carried out to increase a hermetic reciprocating compressor's life expectancy and efficiency.

The scope of the current study includes development of a pump that could supply the lubrication oil between piston and cylinder clearance at low speed for an inverter-type hermetic reciprocating compressor. This way the friction will be reduced, and the efficiency of the compressor will enhance. The other way to lower the friction between piston-cylinder contact and to enhance the tribological performance of the hermetic compressor is to apply micro-textures on the piston upper bearing and skirt. Moreover, the development of new material which will be wear-resistant and lighter in weight for the piston of the compressor is also included in the scope of this work. The following are the key aims of this thesis.

- To study the micro-textured piston effect on the performance coefficient of a refrigerator compressor.
- Developing a pump to solve the lubrication problem of a refrigerator compressor for low-speed operations.
- Manufacturing of a lightweight piston for the hermetic reciprocating compressor from Al_2O_3-Al cermet material using additive manufacturing technique.
- Finally, to underline the problems faced during this research and put forward recommendations for potential work.

1.6 Thesis outline

The thesis discusses three different ways to enhance the energy performance of a hermetic reciprocating compressor i.e., by creating micro-texture on the piston surface, developing a unibody pump for better lubrication at low speed, and manufacturing the lightweight piston from a cermet material via negative additive manufacturing technique.

The thesis consists of five sections. Chapter 2 puts out the background, literature review, and study of surface texture on the hermetic reciprocating compressor piston and discusses the textured piston effect on the performance of a compressor and its characterization. Chapter 3 discusses the development of a unibody pump for the lubrication of a refrigerator compressor at low speeds. Chapter 4 discusses the negative additive manufacturing of pistons from a cermet material using a multi-material 3D printing methodology. Finally, chapter 5 supports the conclusion and offers opportunities for potential work.

Chapter 2

LASER SURFACE TEXTURING ON THE PISTON OF COMPRESSOR

2.1 Introduction

Increasing the coefficient of performance (COP) of a hermetically sealed reciprocating compressor is the most vital challenge for the refrigerator manufacturing industry [1]. The COP of the cooling appliances is clearly associated to the performance of the compressor. Depending on the cooling capacity, inverter-type hermetic reciprocating compressors operate at a wide range of rotational speeds (900 rpm – 4500 rpm). The lubrication oil in all the compressor bearings specifically for the piston-cylinder contact may change significantly during the startup, peak time, and shutdown of the compressor. Since the majority of the energy losses occurred at piston-cylinder contact, adequate lubrication should be provided there to lower the friction and wear and enhance the COP of the compressor [2]. The friction coefficient of this system strongly depends on the load and speed of the hermetic compressor [3]. To improve the COP of the inverter-type hermetic reciprocating compressor, it is much necessary to lower the friction coefficient between piston-cylinder pairs over a wide range of speed and load. Maintaining a sufficient lubrication oil layer between the cylinder and piston at a broad range of compressor speeds is quite challenging for an inverter-type hermetic reciprocating compressor.

One way to lower the friction between piston-cylinder contact and to enhance the tribological performance of the system is to apply micro-textures on the piston upper bearing and skirt [4–7]. Previous research have shown that micro-texturing enhances the performance of a system by changing the lubrication condition from boundary lubrication to hydrodynamic lubrication [8,9]. Micro-texture on the piston surface not only could enhance the hydrodynamic pressure under full film lubrication but also can act as lubrication oil reservoirs under starving conditions [10–14]. In addition, micro-texture could also be used for trapping the wear debris during a long-run operation of the hermetic reciprocating compressor which can contribute to the durability of the compressor. Micro-texturing can also reduce wear and friction by reducing the contact area between sliding bodies [15–18].

Over the past few decades, various techniques have been developed for micro-texturing including laser surface texturing (LST) [19,20], micro-milling [21,22], micromechanical texturing [23], shot blasting [24], diamond embossing [25], micro-casting [26,27], reactive ion etching [28–30], and pulsed air arc treatment [31]. All of them have their own pros and cons and the selection of the technique mainly depends on the application and material. Laser surface texturing has been used in this study because of its adaptability, excellent control, and repeatability. LST process uses high-energy pulses to ablate material by rapid melting and vaporizing above the threshold fluence and the threshold mainly depends on the material microstructure, morphology, as well as laser pulse duration, and wavelength. The most important parameters in surface texturing are depth, width/diameter, orientation, and area density [32,33].

In the literature, there are many studies on computational fluid dynamics to observe the lubrication oil flow over micro-textures [34–36]. However, the majority of the work performed with micro-texturing is experimental due to its complexity under boundary/mixed or starved conditions. An experimental study was carried out by Surya et al. [37] to study the tribological benefits of various laser surface textures under realistic operating conditions of starved lubrication by measuring the friction coefficient. They produced micro-dimples on a flat metallic surface and measured the coefficient of friction by a pin on a disk tribometer. In another study, Miki Nakano et al.[38] fabricated micro-textures on the cast-iron surface via the shot blasting method and investigated the friction coefficient by tribometer. Recent studies have considered the optimization of micro-textures for bearings and piston rings. Researchers studied the effect of micro-texture depth on the coefficient of friction [39,40].

Regardless of the tremendous advantages of the micro-textures, the effect of the micro-textured piston on the coefficient of performance of the hermetic reciprocating compressor has not been studied so far. The main aim of this study is to create micro-textures on the actual piston of the hermetic reciprocating compressor and investigate the effect on COP, and refrigerant leakage.

2.1 Materials and methods

In this research, the compressor of concern is an inverter-type hermetic reciprocating compressor for domestic applications which is shown in Figure 2.1.

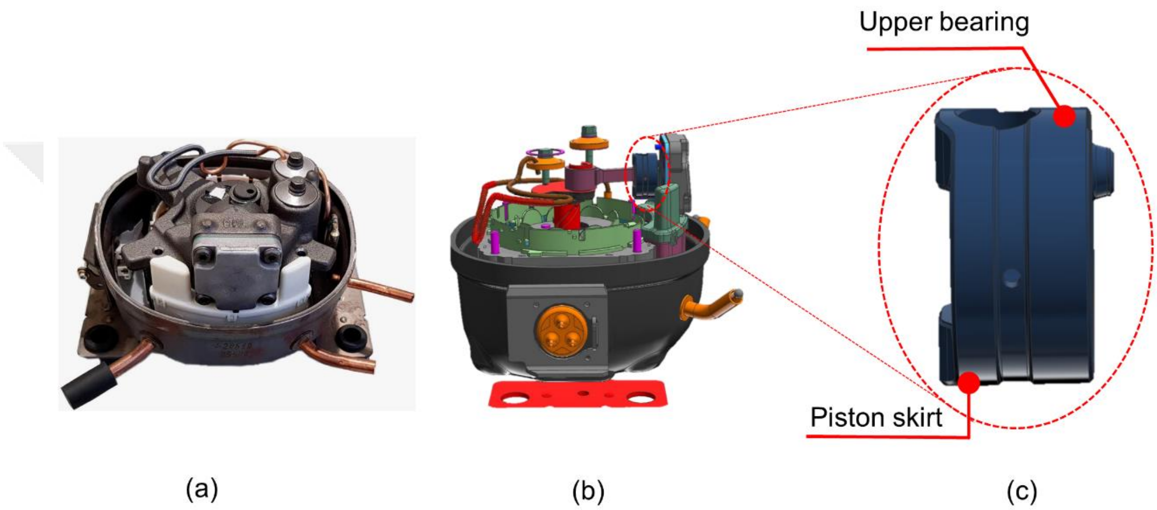

Figure 2.1 a) Image of inverter-type hermetic reciprocating compressor (b) CAD model (c) Piston

Subjected to the refrigeration capacity, this compressor operates at various rotational speeds (N) i.e., 1200-4500 rpm. It has a cooling capacity of 173 W at a speed of 3000 rpm. The piston is made of medium carbon steel by sinter powder metallurgy. The microhardness of the piston samples was measured by using a Vickers hardness tester (Shimadzu HMV-G Series microhardness tester, Japan) before the laser surface texturing. A load (F) of 0.98 N was applied using a diamond indenter for a time of 10 seconds. Overall, five indentations were created, and the average micro-hardness value was found to be 220 ± 20 HV.

AμFAB laser system used in the fabrication of micro-textures on the piston produced 120 fs pulses with a wavelength of 800 nm at a repetition rate of 120 kHz. The beam was focused on the piston surface by using a 10x objective. The schematic of the experimental setup used for the laser surface texturing is shown in Figure 2.2.

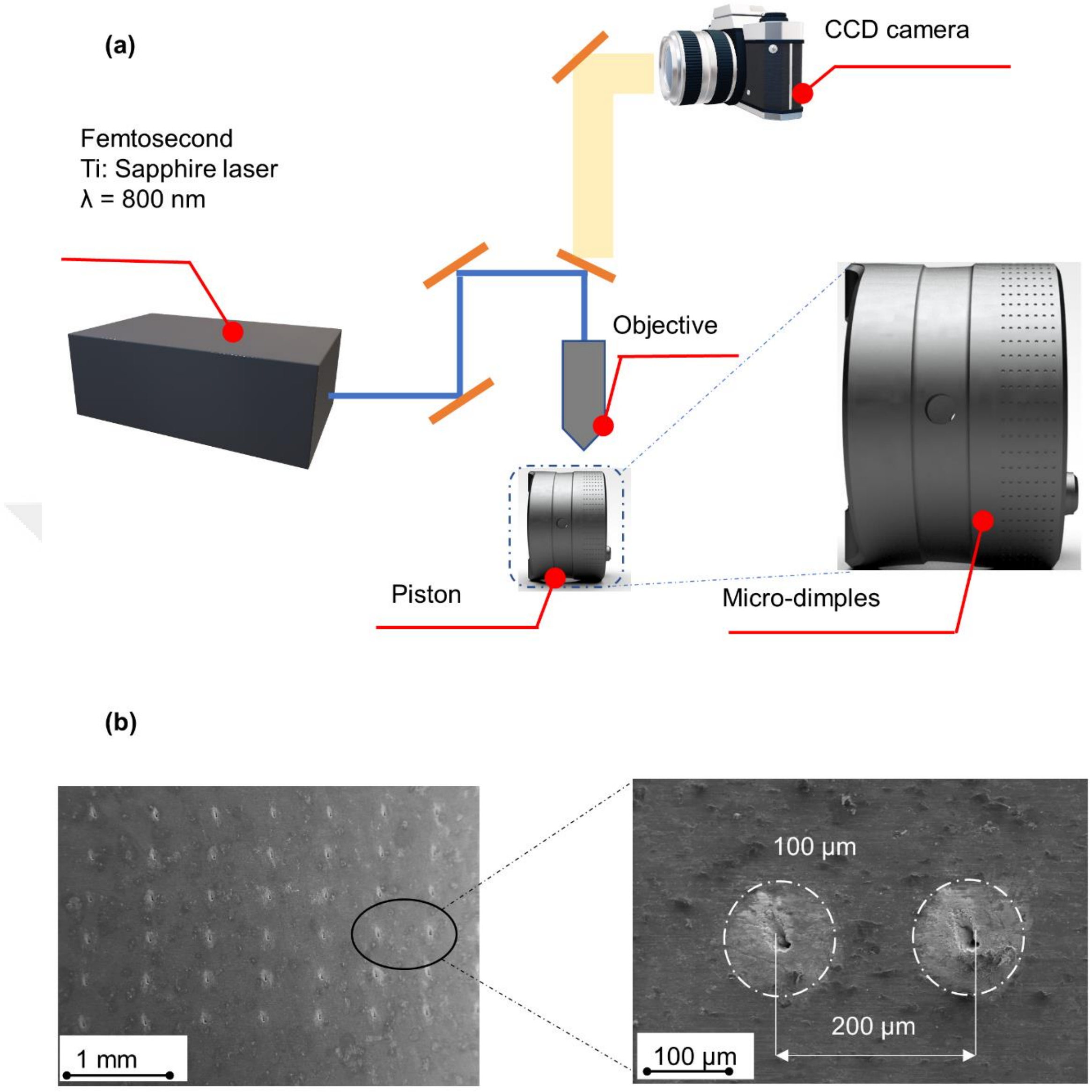

Figure 2.2 Schematic of femtosecond laser micro-texture setup used for piston (b) SEM images of the micro-dimples

First, the laser power was calibrated by finding the threshold fluence of the piston material. There was no ablation observed below 18mW laser power. Since the depth of the texture mainly depends on the laser power, a range of laser power from 18 mW to 60 mW was calibrated against the depth of the texture.

Four different textures were fabricated on the piston (Figure 2.3). Since this micro-fabrication equipment is designed for flat samples only, a separate rig. was designed and installed for cylindrical sample (piston) texturing. Figure 2.4 shows the details of the rig. The details of the texture patterns are shown in Table 2.1.

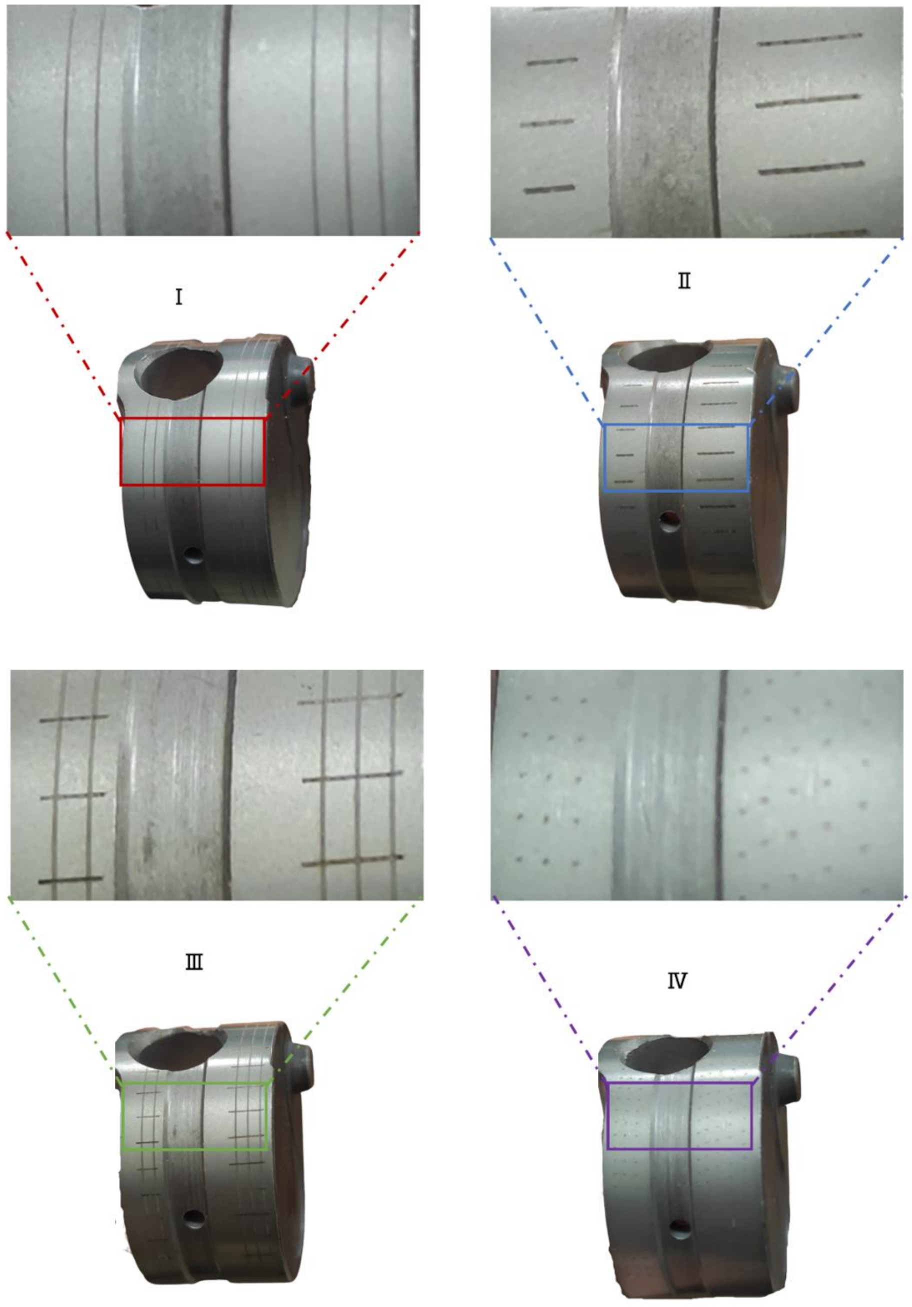

Figure 2.3 Illustration of pistons with various micro-texture (I) radial grooves (II) axial grooves (III) mesh grooves (IV) micro-dimples

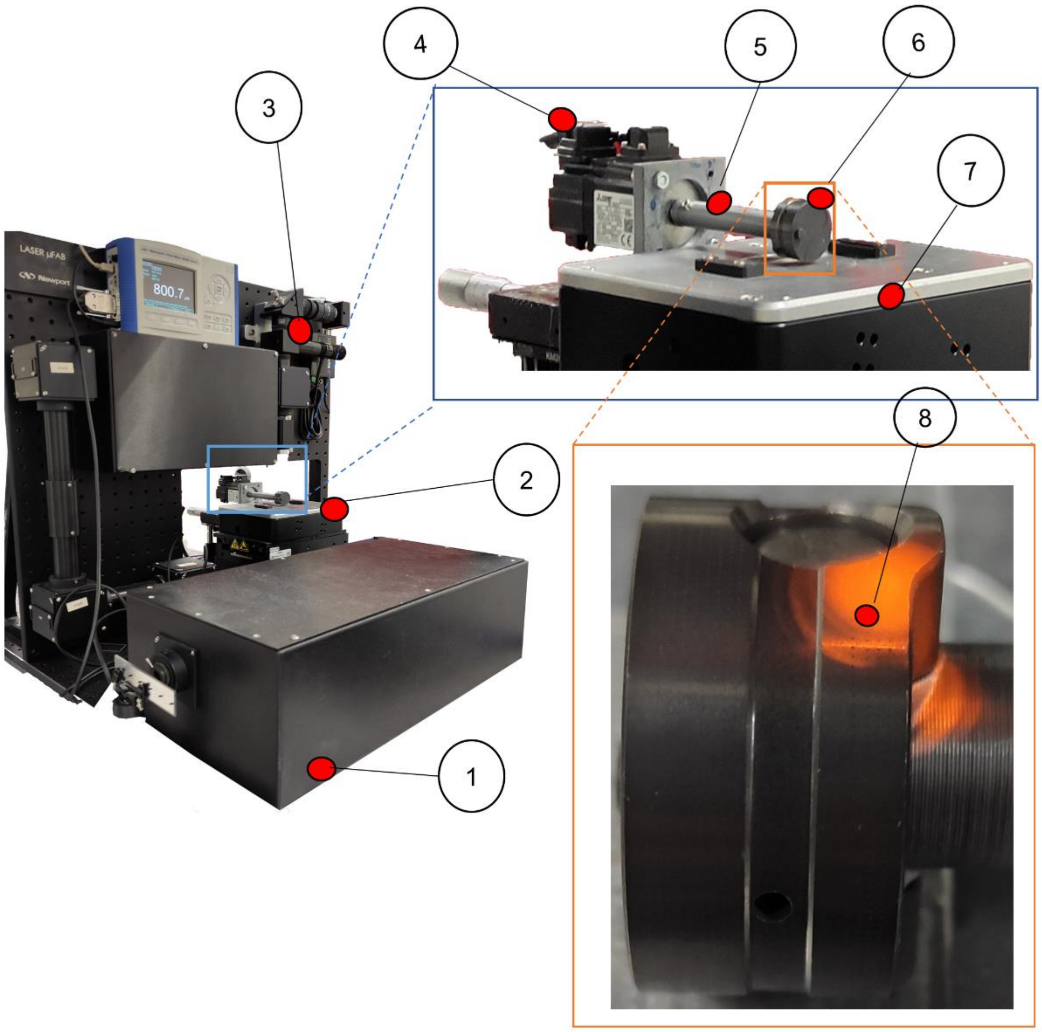

1	Laser attenuator	5	Fixture
2	Servo motor setup	6	piston
3	Objective	7	Micro-meter slide
4	Servo motor	8	Micro-dimples

Figure 2.4 Experimental setup for the micro-texture fabrication on the piston surface

Table 2.1 Details of the micro-texture patterns

Pattern designation	Shape	Width/Diameter (µm)	Depth (µm)	Pitch (µm)	No. of grooves	Area Density (%)
U	Untextured	-	-	-	-	-
R1	Radial groove	100	5-8		1	
R2	Radial groove	70	5-8	500	3	
R3	Radial groove	70	15-20		1	
R4	Radial groove	100	5-8	500	5	
A1	Axial groove	100	5-8	500		
A2	Axial groove	100	15-20	500		
A3	Axial groove	70	5-8	500		
A4	Axial groove	70	15-20	500		
M1	Mesh groove	100	5-8	500		
M2	Mesh groove	100	15-20	500		

M3	Mesh groove	70	5-8	500	
M4	Mesh groove	70	15-20	500	
D1	Micro-dimple	100	5-8		20
D2	Micro-dimple	100	15-20		5
D3	Micro-dimple	100	15-20		20
D4	Micro-dimple	100	5-8		5
D5	Micro-dimple	70	15-20		5
D6	Micro-dimple	70	5-8		5

Since theoretical modeling for the starved condition lubrication in the case of a hermetic reciprocating compressor does not exist in the available literature, a set of experiments was designed based on the physical understanding to explore the consequence of creating micro-texturing on the piston of a hermetic reciprocating compressor. For radial, axial, and mesh micro-grooves, four types of texture were created whereas for the micro-dimple six types of texture were achieved and investigated.

The piston was mounted on a servo motor via a fixture and the motor was fixed to a micrometer slide. The rotation of the piston was monitored and controlled with a computer-controlled servo motor.

Figure 2.5 shows scanning electron microscopy images of the patterns. It should be noted that radial grooves, perpendicular to the motion of the piston, were prepared with a width of 100 micrometers (a, b). Axial grooves, parallel to the piston motion, were prepared with the same width (c, d). Mesh grooves which are a combination of radial and axial grooves were also prepared (e, f). Lastly, micro-dimples with a diameter of 100 micrometers are shown in (g, h). The width of the radial, axial, and mesh groove and the diameter of the circular micro-dimple depends on the lense of the μFAB laser system. In this study, two lenses were used i.e. 70 and 100 microns. It is worth mentioning that focus of the beam is very important to fabricate smooth and homogenous texture. The SEM images shows a homogeneity and uniformity in the formation of the micro-texture. The white light interferometry (WLI) technique was employed to measure the depth of the textures.

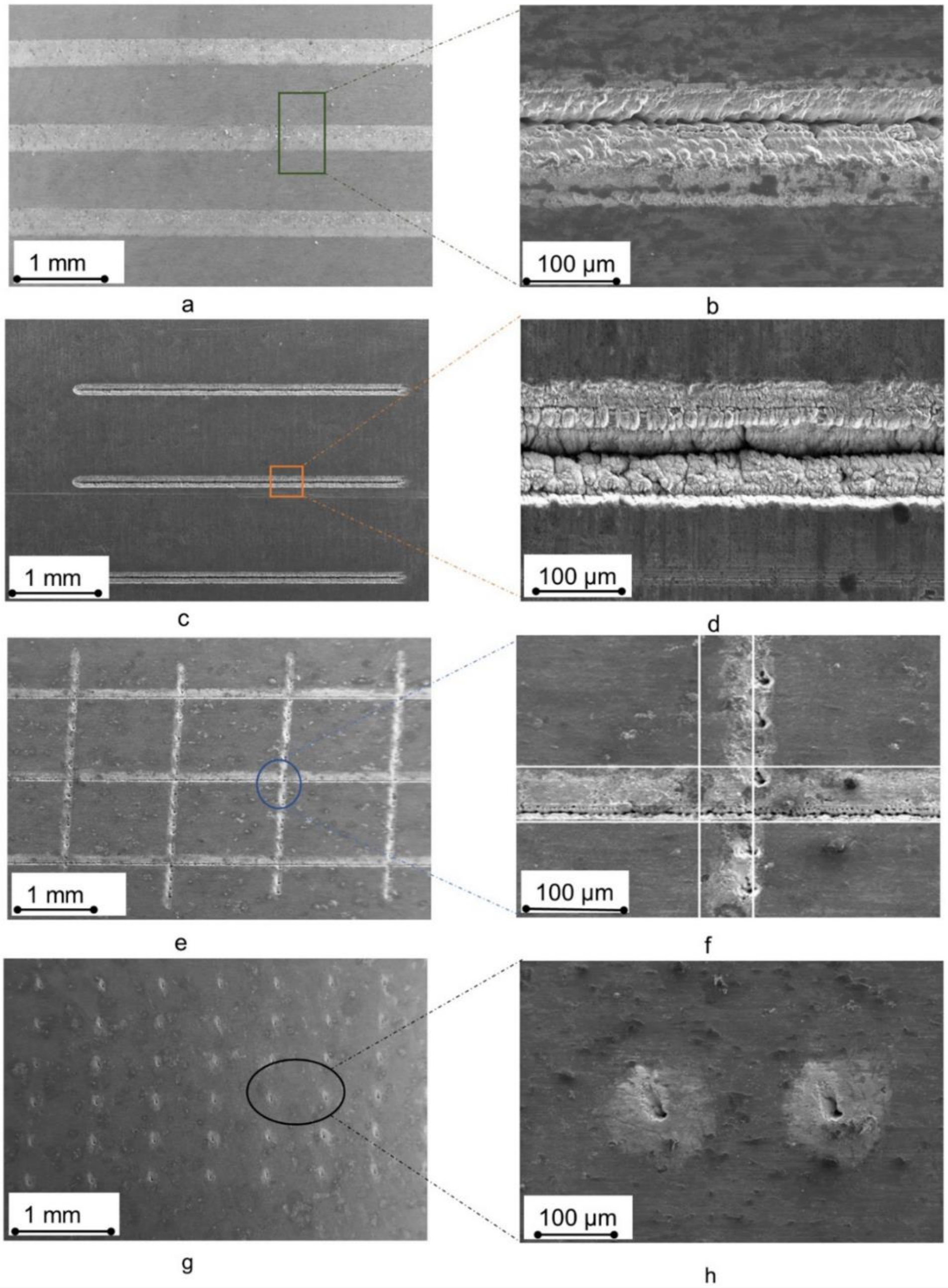

Figure 2.5 SEM images of the piston textures (a, b) radial grooves (c, d) axial grooves (e, f) mesh grooves (g, h) micro-dimples

Figure 2.6 shows the depth of the textures. Two depths were studied for all the textures. With the high power possible of the laser, a maximum of 15-20 micrometers depth was achieved whereas with a low laser power 5-8 micrometers depth was produced. It can be seen from the WLI results that the average depth of one of the micro-textures is 15-20 micrometers. The depth of the texture totally depends on the power of the µFAB laser system. The μFAB laser system employed in this study has a power range of 1-1000 μW. Before creating the micro-texture, various powers were calibrated againt the depth of the texture on the piston surface. The minimum power threshold for a medium carbon steel piston was found to be 700 μW.

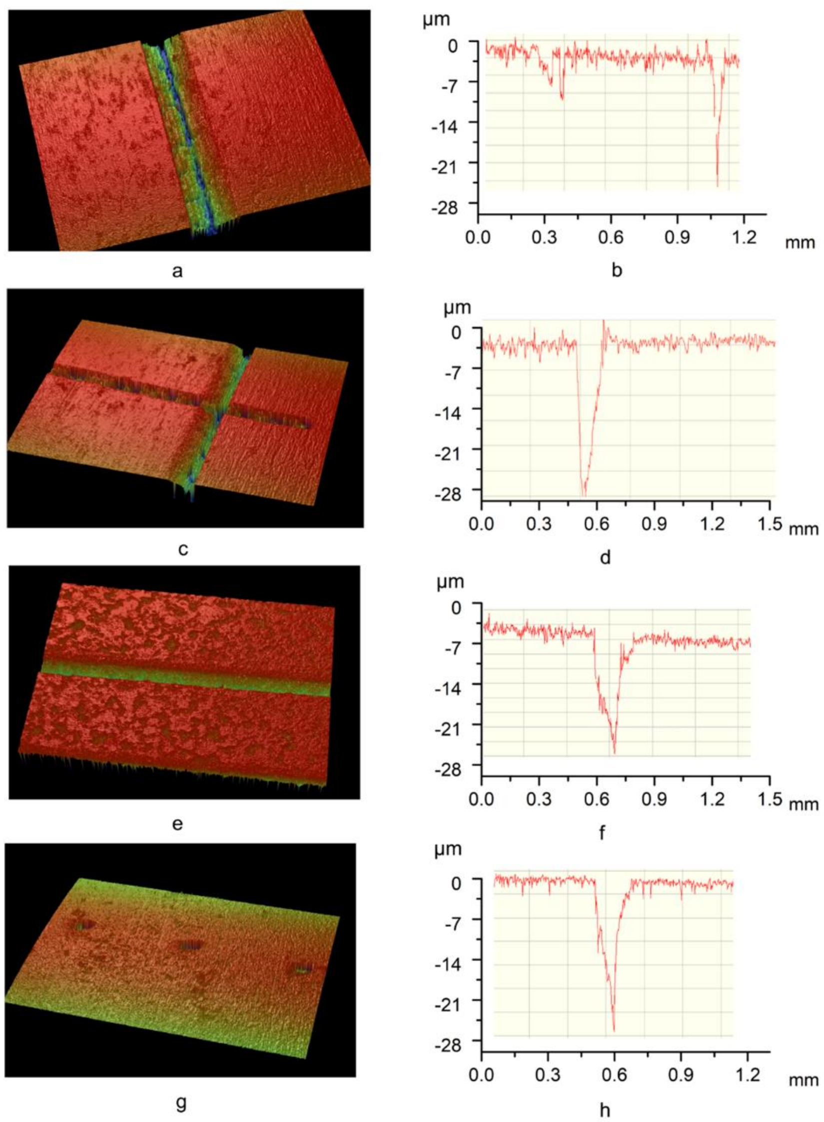

Figure 2.6 White light interferometry results, showing the average depth of the texture piston textures (a, b) radial grooves (c, d) Mesh grooves (e, f) axial grooves (g, h) micro-dimples

2.2 Results and discussion

A calorimeter facility was employed to study the COP of the compressors at ASHRAE conditions. The properties of the commercially available lubrication oil employed in this study are recorded in Table 2.2.

Table 2.2 Properties of the lubricating oil (VG 5)

Temperature, T, (°C)	20	40	60
Density, ρ, (kg m^{-3})	852	840	827
Kinematic viscosity, v, (mm^2 s^{-1})	12.7	7.5	4.6

Figure 2.7 shows the COP of all the tested compressors comprising untextured and micro-textured pistons at three different rotational speeds i.e., 1300 rpm, 3000 rpm, and 4500 rpm. The results of textured pistons were compared with the untextured piston compressor. Each texture was tested on the three pistons to minimize the error, the plot signifies the average COP, and the error bar reveals the maximum and minimum COP values.

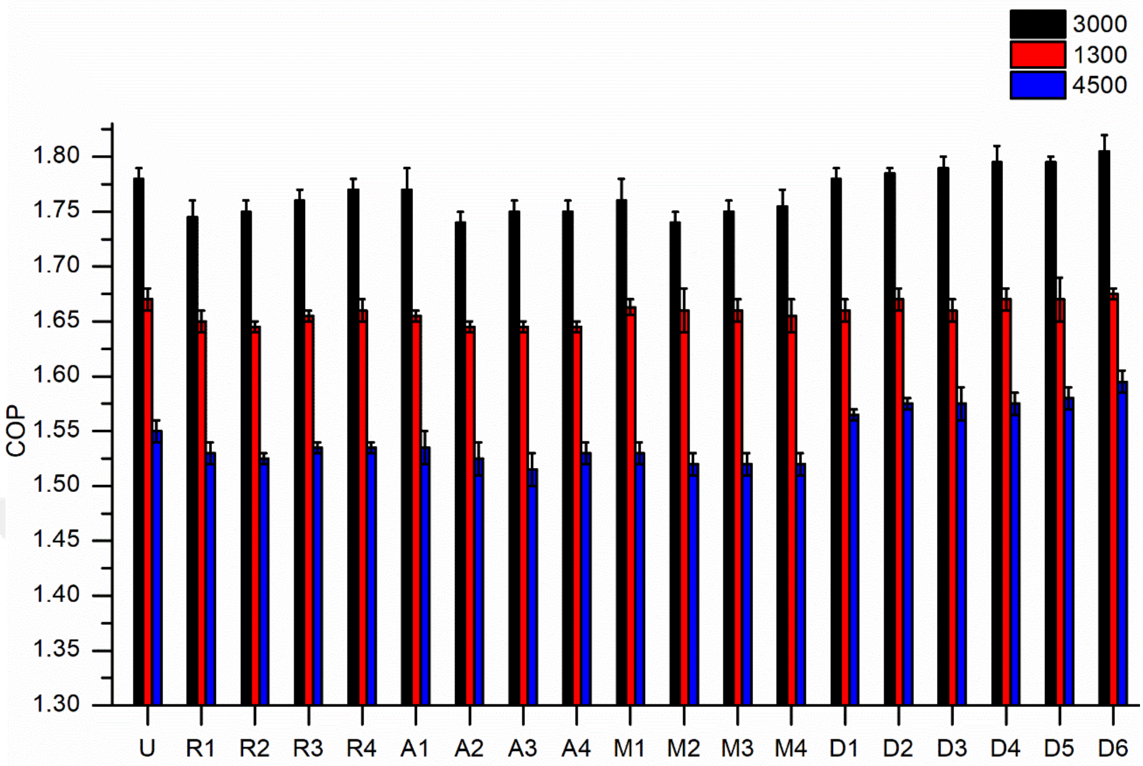

Figure 2.7 Comparison of Coefficient of performance for the untextured and textured patterns investigated under equal conditions

The variation of the coefficient of performance (COP) values of the hermetic compressors with different micro-texture patterns and untextured pistons with different rotational speed of the compress is presented. The results signifies that the coefficient of performance decreases when the speed is either too low (1300 rpm) or too high (4500 rpm). At the lower rotational speed of the hermetic compressor, although the micro-texture patterns exhibited marginally lower COP values than the untextured surfaces, the difference was trivial. Moreover, the COP values of all the textured patterns were relatively identical, showing that the effect of texture on the piston surface was not significant at lower rotational speeds i.e., 1300 rpm. Therefore, the benefits of introducing micro-texture at lower rotational speeds (less aggressive) are not significant. Nevertheless, as the rotational speed of the compressor was increased, the operating conditions became more aggressive, and the effect of micro-texturing became clearly noticeable. Compared to 1300 rpm, at 4500 rpm speed, the micro-dimpled piston performed remarkably well. Also, the COP of the compressors is different for each micro-texture shape at 3000 rpm and 4500 rpm which shows a strong impact of the micro-texture geometry on the performance at higher rotational speeds, with D6 performing the best at higher speeds.

Based on the above results, the fabrication of micro-dimples on the piston surface has a significant tribological benefit and positive effect on the COP of a hermetic reciprocating compressor. However, axial, radial, and mesh grooved pistons led to a lower value of the compressor’s COP as compared to untextured piston compressors.

In contrast to continuous micro-grooves (axial, radial, and mesh), micro-dimpled pistons performed comparatively better in terms of coefficient of performance. Experiments were carried out with various dimple diameters, depths, and area densities from D1-D6. Micro dimples with an area density of 5%, a diameter of 70 microns, and a depth of 5-8 microns showed the highest COP as compared to the rest of the micro-dimpled patterns. Although the D6 pattern is the shallowest and had low lubrication oil storage ability, however, because of low area density, the wear debris at the interface between piston and cylinder would also be the lowest which led to the higher coefficient of performance as compared to D1 which had area density of 20%. The tribological performance of the piston got worse as the area density of the micro-dimples increased: an area density of 5% was found to be improved than 20%, under the same ASHRAE testing conditions.

Figure 2.8 summarizes the results and shows the results of texture which performed best among its peers. Pattern Ⅰ which corresponds to R4, represents the radial micro-grooves having a width of 100 micrometers and a depth of 5-8 micrometers. The total number of grooves was five (three on the upper bearing of the piston and 2 on the lower skirt) with a pitch of 500 micrometers. Pattern Ⅱ and Ⅲ which correspond to A1 and M1 represents the axial and mesh micro-grooves respectively having the same width, depth, and pitch as R4. Pattern Ⅳ corresponds to D6 and represents micro-dimples with a diameter of 70 micrometers and 5-8 micrometers depth with an area density of 5%.

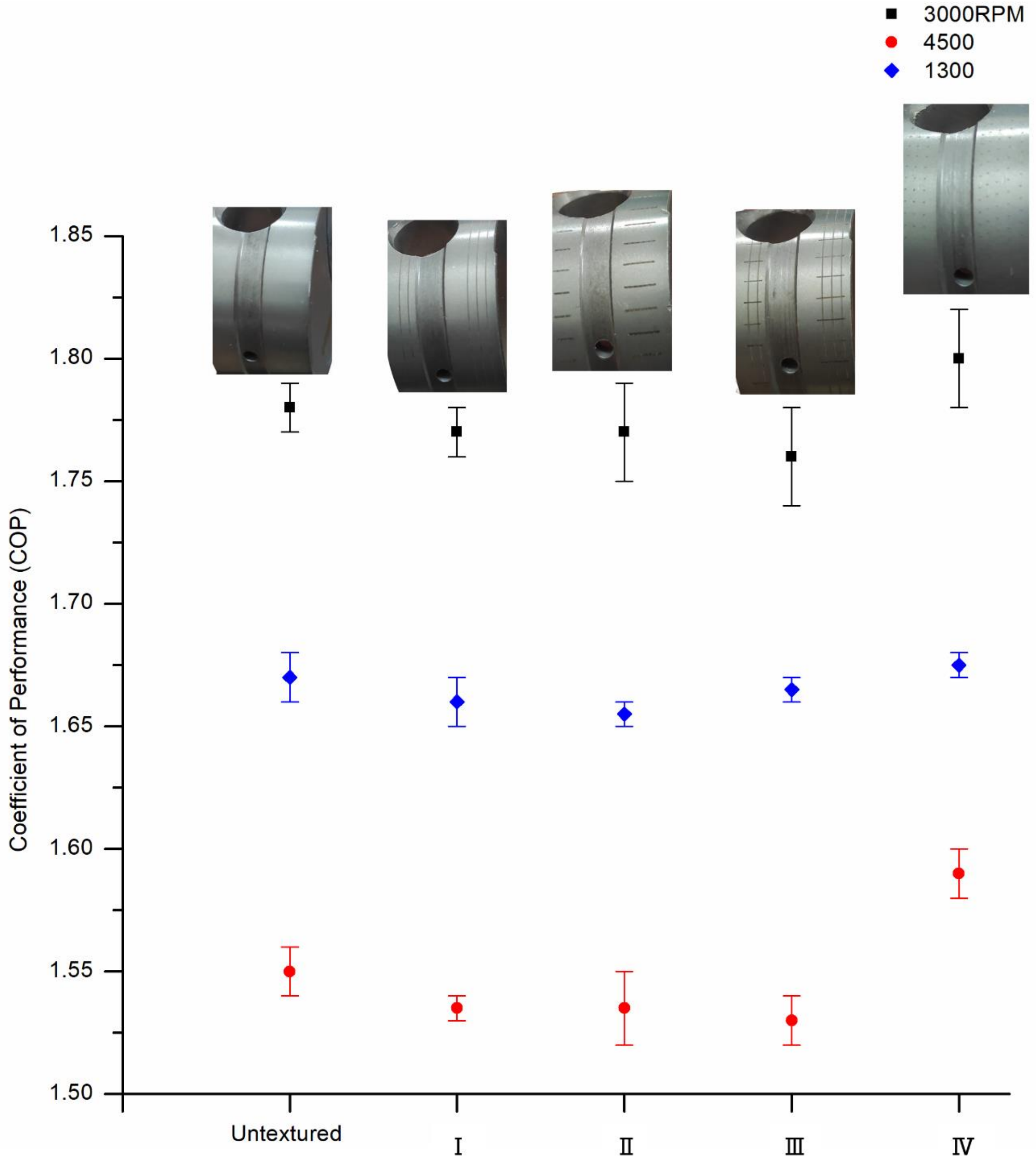

Figure 2.8 Coefficient of Performance of the compressor with various textured pistons at different speeds

It is obvious that texture Ⅳ performed best among all the textures, and displays a relatively high level of COP.

Lower values of COP in the case of patterns Ⅰ, Ⅱ, and Ⅲ could be explained by the continuous depression area which could possibly cause high friction. The majority of the lubrication oil was captured by the continuous grooves due to which the thickness of the lubrication oil between the piston and cylinder was reduced. Therefore, the lubrication condition tended to be a boundary lubrication state, in which the asperity contact is more server.

Higher values of COP for micro-dimples pattern Ⅳ could be explained by the variation of hydrodynamic pressure. Due to an increase in the hydrodynamic pressure near the micro-dimple area, the load-bearing capacity and thickness of the lubrication film increase. This phenomenon was also studied by Ronen et al.[11] and Etsoin et al. [33] It was reported that the hydrodynamic pressure increases in the vicinity of the micro-dimples and thus friction force reduces. In the literature, numerous studies prove that during the reciprocating motion, micro-dimples expand the range of hydrodynamic lubrication regime and reduce the friction coefficient between sliding bodies.

It should also be noted that no significant wear occurred during testing. It was observed that after testing the compressors for 2 hours the micro-textures were still present on the piston surface.

The results of the cooling capacity (Q_c) and power (P) intake for the compressors with untextured and textured pistons are shown in Figure 2.9.

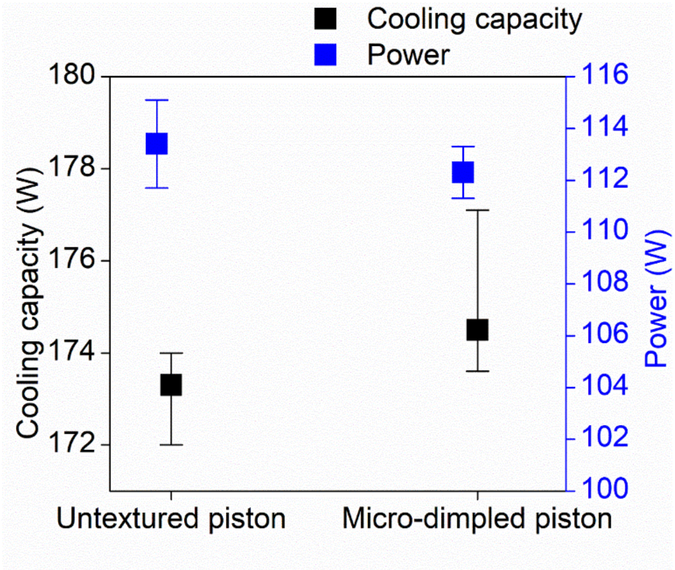

Figure 2.9 Cooling capacity and power intake for the untextured and textured piston compressors

The average cooling capacity of the compressor with an untextured piston was observed to be 173.4 W with an average power intake of 113.4 W. Contrary to this, the compressor with the micro-dimpled piston displayed a 174.5 W average cooling capacity with an average of 112.8 W power intake.

A static refrigerant leakage test was conducted on the compressors with textured (micro-dimples) and untextured piston compressors where a maximum of 15 bar pressure was achieved by running the compressor and shutting the outlet of the compressor using a valve. Refrigerant leakage test results are shown in Figure 2.10.

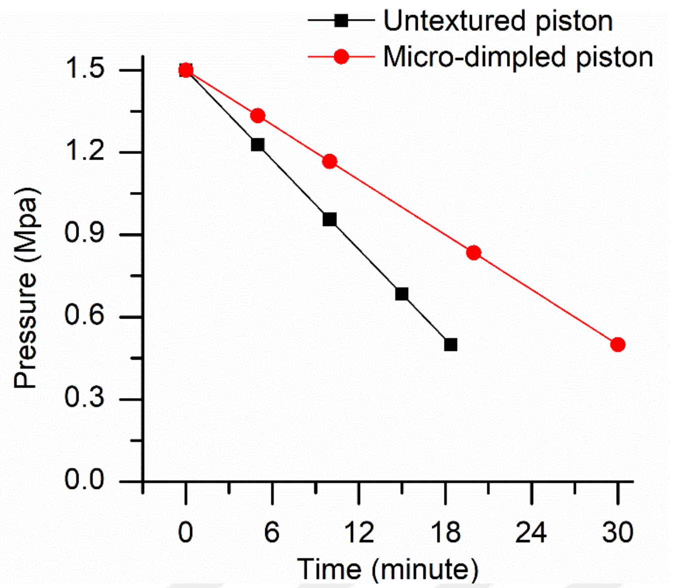

Figure 2.10 Refrigerant leakage test results for textured (TEXTURE IV) and untextured piston compressors

The outlet pressure was measured using a barometer and the compressor was stopped when the pressure reached 15 bars. Then the pressure was allowed to drop because of the leakage. The pressure drop from 15 bar to 5 bar was observed to be 35% slower in the case of textured piston compressors as compared to untextured piston compressors.

The gap between the piston and cylinder for a hermetic reciprocating compressor is usually around 5-10 micrometers. Refrigerant leakage through this clearance reduces performance by the reduction of capacity and by the power expenditure of lost refrigerant. In hermetic reciprocating compressors, this clearance is filled with lubrication oil. Other than its lubricating role, the lubrication oil also acts as a sealing for the piston-cylinder clearance [41–44]. From the results (Fig. 2.10) micro-dimples on the piston surface could greatly decrease the refrigerant leakage through the piston-cylinder clearance. This can be explained by the phenomenon that micro-dimples act as lubrication reservoirs and during the operation a thick film of lubrication oil inhibits the refrigerant leakage from the piston-cylinder clearance. Generally, micro-texture on the sliding surface has positive effects such as oil storage, wear debris accumulation, creating a hydrodynamic, pushing-up force, and minimizing the surface contact area. The performance of a micro-dimpled texture is characterized by the integrated effect of those mechanisms. Nevertheless, under various solid contact conditions, each mechanism has its own importance. For example, under hydrodynamic lubrication, which has no solid contact at the friction interface, micro-texture on the surface can lead to an increase in the load-carrying capacity of the lubricant film. Therefore, lubrication conditions could be the major factor that defines the functioning of micro-textures.

2.3 Conclusion

In summary, through the experimental study carried out in this work, it can be summarized that surface texturing on the piston has a great potential for application in hermetic compressors to enhance the coefficient of performance (COP) of the compressor. In addition, the textured piston has a significant effect on the refrigerant leakage of the hermetically sealed compressor. The micro-texture on the piston surface was prepared by the laser surface texturing method. Four types of micro-texture were studied: radial micro-grooves, axial micro-grooves, mesh micro-grooves, and micro-dimples. It was found that the radial, axial, and mesh micro-grooves piston negatively affect the coefficient of performance (COP) of the hermetic reciprocating compressor. However, the piston with the micro-dimple texture significantly (1%) increased the compressor's coefficient of performance. Refrigerant leakage from the piston-cylinder clearance was observed to be 35% less in the case of the micro-dimpled piston due to the presence of a continuous oil film between the piston and cylinder. In addition, the cooling capacity of the compressor with a micro-dimpled piston increased by 1 W as compared with the non-textured piston compressor.

Chapter 3

UNIBODY AXIAL FLOW PUMP

3.1 Introduction

A hermetic reciprocating compressor is the core element of the household cooling system, and its lubrication is a critical issue because lubrication is directly associated to wear, reliability, and mechanical losses of the compressor [45]. Studies show that friction and wear in a hermetic compressor moving parts have a crucial impact on the overall coefficient of performance of the refrigeration cycle [46,47]. It is likely to reduce friction and wear by providing sufficient lubrication to all moving parts of the compressor during the operation [48]. After the compressor start-up, immediate and sufficient availability of lubrication oil to the hydrodynamic bearings and the piston-cylinder space plays a crucial part in the refrigeration cycle efficiency [49]. The lubrication oil supply system of a hermetic reciprocating compressor mainly based on the crankshaft which plays the role of an oil pump [50]. In a hermetic domestic refrigerating compressor, the lubrication oil supply system is commonly provided by an integrated pumping system on the crankshaft which consists of a centrifugal pump and helical channels on the crankshaft [51]. It is assumed that the lubrication oil rising from the compressor sump to the helical channel is purely due to the centrifugal forces [52]. The centrifugal pump is partially immersed into the lubrication oil sump at the bottom of the shell and when the crankshaft rotates, the oil in the sump is pumped into the centrifugal pump and delivered to the crankshaft helical channel. This process provides lubrication to all moving parts and hydrodynamic bearings of the hermetic reciprocating compressor [53]. The lubrication oil not only carries heat from the high-temperature regions to the shell but also, most importantly, it acts as sealing between the piston and cylinder to minimize refrigerant leakage and to enhance the coefficient of performance [54].

In the literature, there are many numerical models and experimental findings for the lubrication oil systems of a hermetic reciprocating compressor [55–59]. In one of the studies [50], the effects of oil viscosity and the crankshaft rotational speed on the mass flow rate of the lubrication oil were studied both numerically and experimentally. It was found that the mass flow rate of the lubrication oil mainly depends on the temperature of the lubrication oil i.e., it is decreased at a lower temperature due to a fall in the viscosity value.

The impact of the crankshaft speed on the mass flow rate of the lubrication oil was studied by [46] and it was found that the mass flow rate of the lubrication oil is directly proportional to the speed of the crankshaft in a linear manner due to centrifugal forces. It was also observed that steady-state condition was taking long to achieve at a speed less than 2000 rpm. The relationship between the rising time of the lubrication oil and the crankshaft speed was investigated by [49] by using a high-speed camera. It was found that the crankshaft rotation speed at high values does not have a substantial influence on the rising time, but it can greatly affect the overall mass flow rate of the lubrication oil.

For a regular hermetic compressor that always runs at a higher speed (> 3000 rpm), these two integrated pumps work effectively. However, when it comes to the inverter type or variable speed hermetic reciprocating compressor, providing and maintaining the lubrication oil at a lower speed (<2000 rpm) of the crankshaft is challenging since the lower centrifugal pump cannot raise the lubrication oil to the helical channel pump on the crankshaft [45]. Wu. W et al. [60] carried out simulation studies on a lubrication oil pump system for hermetic reciprocating compressors and the results showed that the existing design of the centrifugal pump of the crankshaft fails to pump the lubrication oil when the compressor speed is under 2100 rpm.

Alves et al. [59] investigated an eccentric tube centrifugal pump for the hermetic reciprocating compressor. They developed a lubrication oil supply system for the compressor which comprises of a tube with an inclined inlet that was mounted off-center with the crankshaft axis. The inclined pick-up tube was connected to the outer helical groove of the crankshaft. The analytical models for the inclined tube and helical groove were studied separately and were combined via numerical methodology. The steady-state volume flow rate for the whole oil supply system was investigated in their study. They performed the analysis at 3000 rpm speed, and it was found that the pick-up tube with an inclination angle of 60°- 68° and 5-mm diameter showed good results in terms of lubrication oil mass flow rate. In another approach, the researchers designed and developed a screw pump to address the lubrication oil pumping issue at a low speed [45]. A lubrication oil pump system was designed for the hermetic reciprocating compressor which was based on a single screw pump attached to the bottom of the crankshaft. A semi-analytical model was developed for foreseeing the lubrication oil mass flow rate in the screw pump oil supply system. In another study, Ozsipahi et al. [61] analytically investigated a screw pump inside the crankshaft for maximizing the lubrication oil mass flow rate of an inverter-type hermetic reciprocating compressor. The results were compared with the numerical simulations. The effect of rotational speed, oil viscosity, immersion depth, and pitch of helix angle on the mass flow rate of the lubrication oil was studied. It was found that increasing the screw aspect ratio improves the mass flow rate of the lubrication oil up to a certain limit.

In this article, a unibody bladeless impeller axial pump is designed, analyzed, and manufactured to immediately provide the lubrication oil to all parts of the hermetic reciprocating compressor. The pump will be mounted at the lower end of the crankshaft and able to supply the lubrication oil to the helical channel pump at a lower speed (< 2000 rpm) with immediate effect. CFD analysis was carried out to get the optimum helix angle of the pump for the maximum mass flow rate of the lubrication oil. Results are valuable to indicate some design directions of the lubrication oil system of a variable speed hermetic reciprocating compressor to meet low rotation speed conditions.

3.1 Development of unibody axial pump

The unibody axial pump is designed for a domestic compact inverter hermetic reciprocating compressor. The pump consists of four helical flutes created inside the body of the pump. The geometry of the oil pumping system for a hermetic reciprocating compressor is shown in Figure 3.1. The height of the unibody axial flow pump was 30 mm while its outer diameter was 12 mm so that it could rigidly fit into the lower part of the crankshaft and rotate with the same speed as the crankshaft (Fig. 3.1a). The main objective of the pump is to raise the lubrication oil from the oil sump to the inlet of the helical channel machined on the crankshaft (Fig. 3.1b). The unibody pump consists of four inlets and four outlets (Fig. 3.1c).

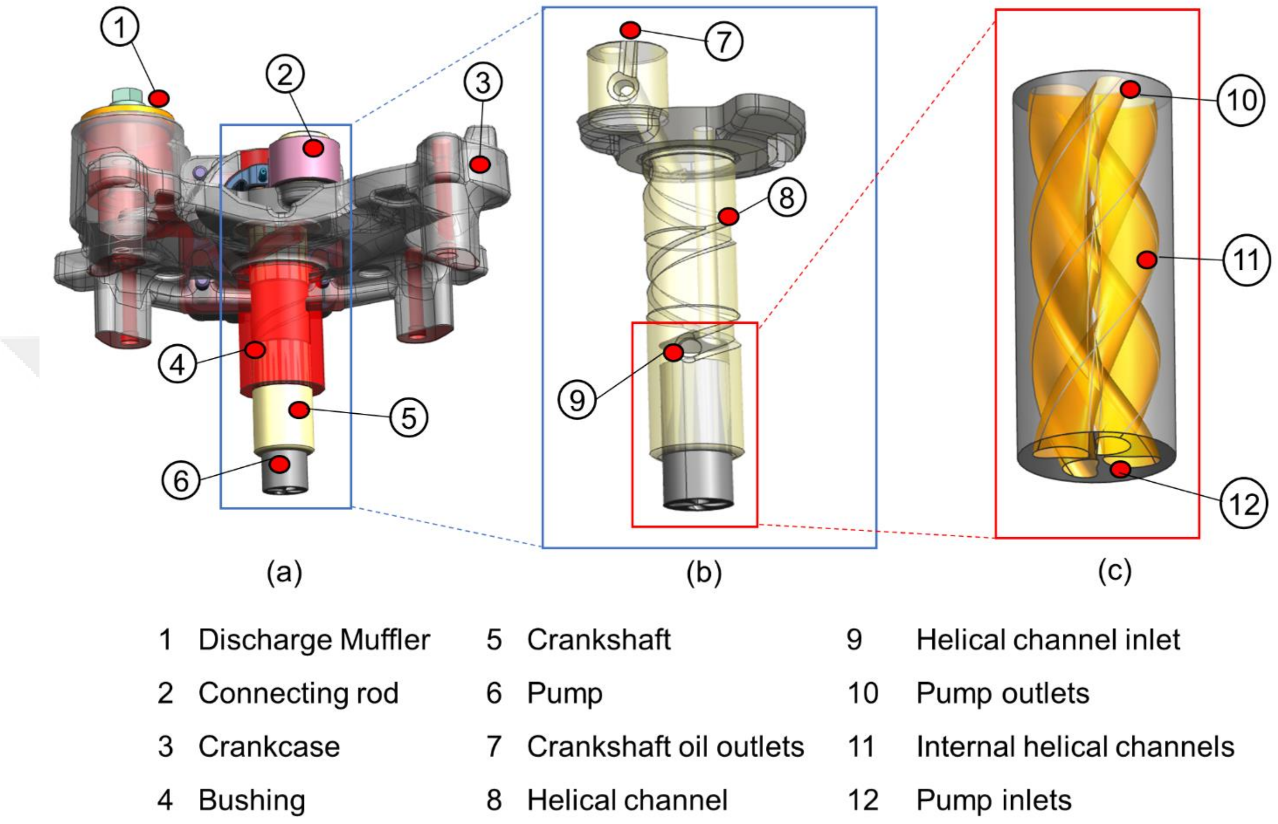

Figure 3.1 Geometry of the pump system. (a) Compressor crankcase with unibody pump attached to the crankshaft. (b) Unibody axial pump inserted in the crankshaft. (c) CAD model of unibody axial flow pump

3.2 Geometry of flutes

A freeform spline geometry was designed for the cross-section of the helical flutes of the unibody axial pump as shown in Figure 3.2.

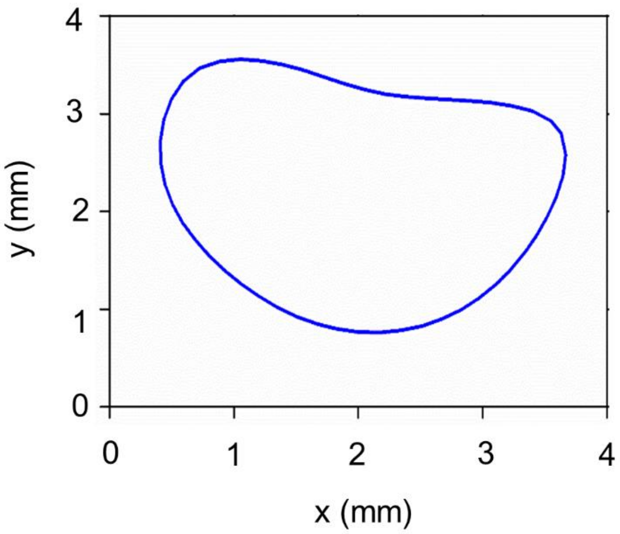

Figure 3.2 Freeform spline geometry of the pump

The geometry was then swept along a helical path with helical angles of 15°, 25°, 35°, 45°, 55°, and 65°. The helical flutes geometries are illustrated in Figure 3.3.

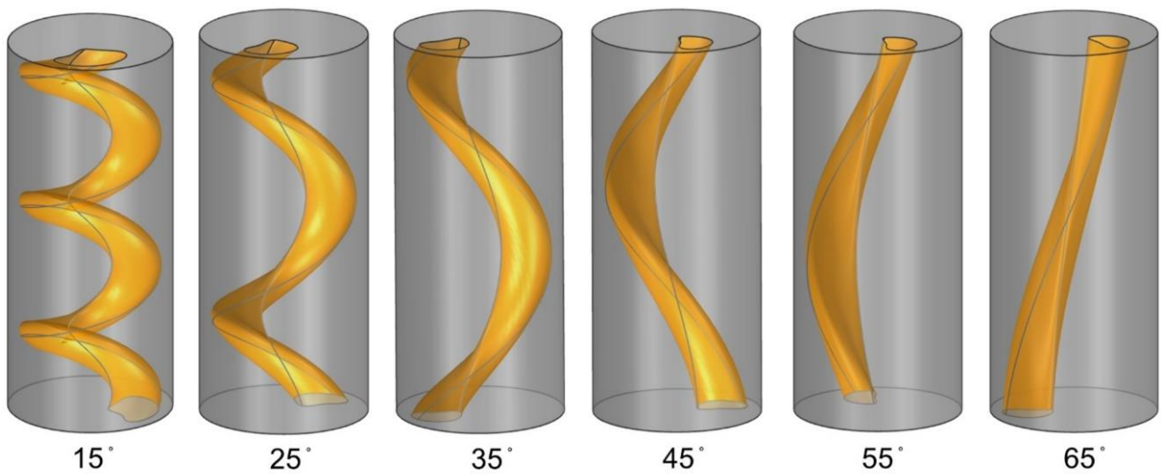

Figure 3.3 Helical flutes of unibody axial flow pump

3.3 Experimental studies

3.3.1 Additive manufacturing of unibody axial pump

The unibody axial flow pump was sliced by a series of parallel planes with a fixed interplane spacing equal to the thickness of the fabrication layer. Pumps with various helix angles were manufactured.

A fused filament fabrication (FFF) head mounted on a Mitsubishi Electric robotic manipulator was employed for the additive manufacturing of the unibody axial pumps. The manufacturing setup is illustrated in Figure 3.4.

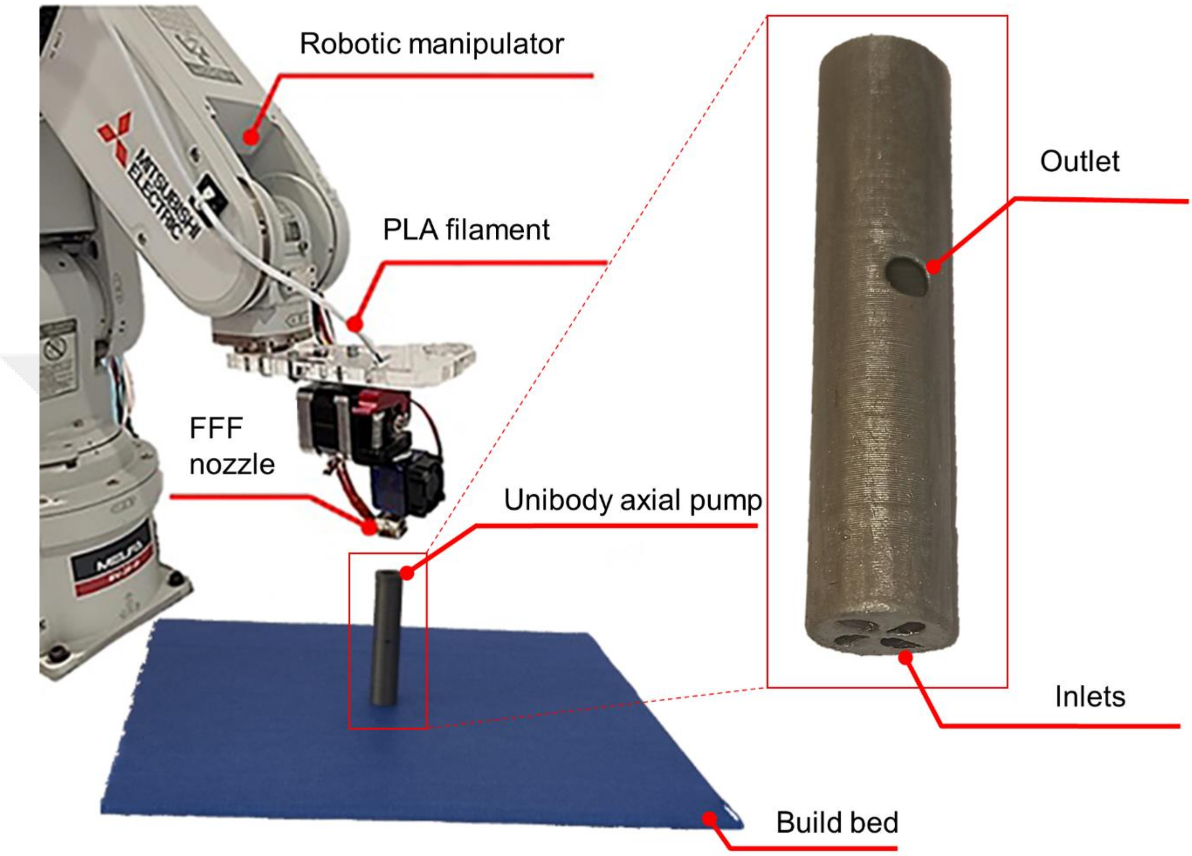

Figure 3.4 Robotic additive manufacturing setup utilized for the manufacturing of test specimen

The unibody axial pump is manufactured from polylactic acid (PLA) by additive manufacturing technique. Since the inner diameter of the lower part of the crankshaft for the studied compressor is 12 mm, therefore, the unibody axial flow pump was designed in such a way that it should snuggly fit into the crankshaft.

3.3.2 Experimental setup

To mount the pump on a servo motor shaft, an extrusion was created on the upper part of the pump and a test rig was prepared to collect the pumped lubrication oil as shown in Figure 3.5.

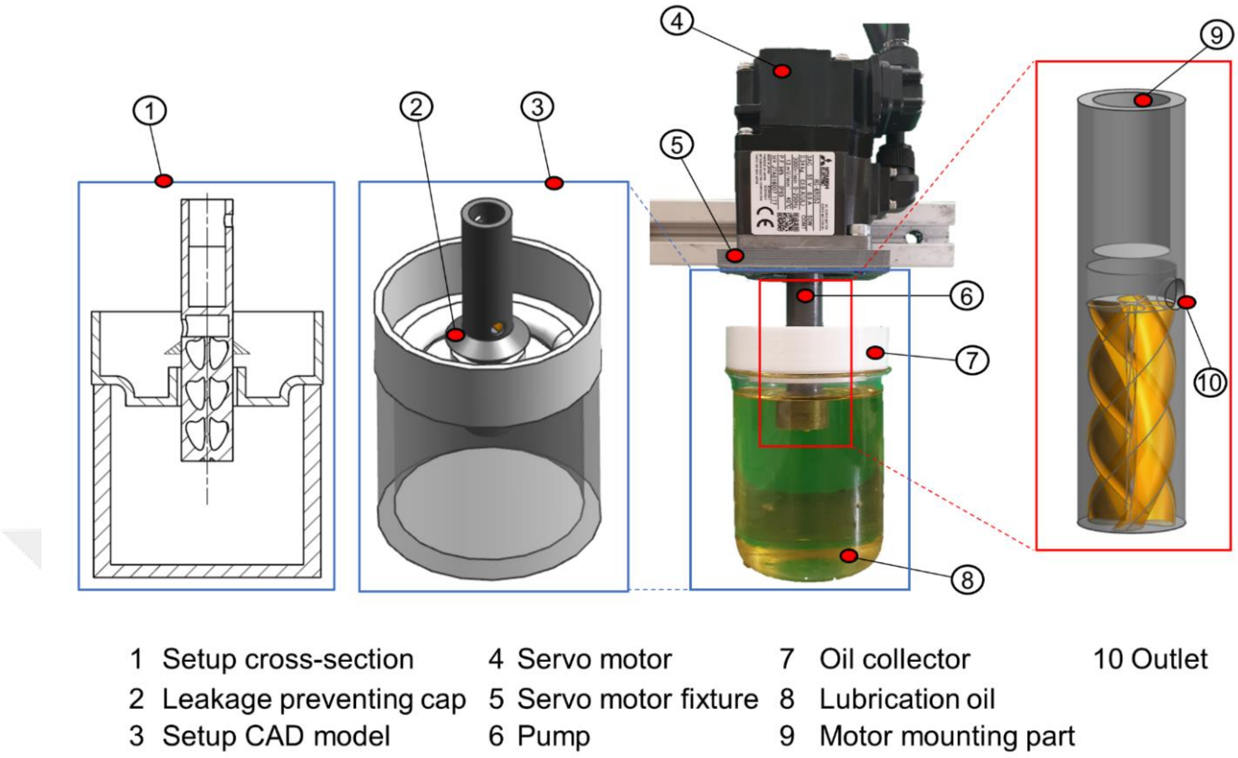

Figure 3.5 Test setup for mass flow rate measurement

The properties of the commercially available lubrication oil employed in this study are registered in Table 3.1.

Table 3.1 Properties of the lubrication oil (VG5)

Temperature (°C)	20	40	60
Density (kg m^{-3})	852	840	827
Kinematic viscosity (cSt)	12.7	7.5	4.6

A collector was placed on top of the sump to collect the lubrication oil. The temperature of the oil sump was measured before and after every reading using a digital thermometer with an accuracy of ±0.3 °C. Each test was repeated 10 times to minimize the experimental errors. Figure 3.6 indicates the repeatability of the measurements at 1800 rpm for a 45° helix angle pump reflected on the standard deviation with 2σ employing 10 measurements for each run.

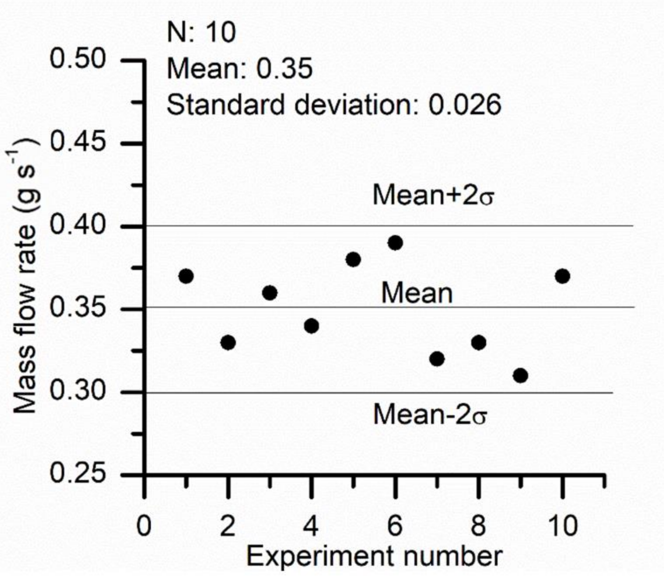

Figure 3.6 Standard deviation of the lubrication oil mass flow rate at 1800 rpm, for a 45° helix angle pump

The repeatability study showed that the standard deviation in the oil mass flow rate was calculated as $\sigma = 0.026$ g s^{-1} from the mean value of 0.35 g s^{-1}. It can also be seen that all the measurements were in the bandwidth of 0.31- 0.39 g s^{-1}.

Each test was performed for 5 s, and the test timing was controlled by the controller of the servo motor with an accuracy of ±10 ms. The pumped oil was collected in a collector and the mass of collected oil was measured using a digital scale with an accuracy of ±0.1 mg.

3.4 Results and discussion

The mass flow rate provided by the unibody axial pump of various helix angles at the speed of 1400 rpm and 1800 rpm is illustrated in Figure 3.7 which shows the comparison of the numerical and experimental results. The simulation was carried out by another MARC fellow, Pouya Pashak. The objective parameter was the pumped oil mass flow rate.

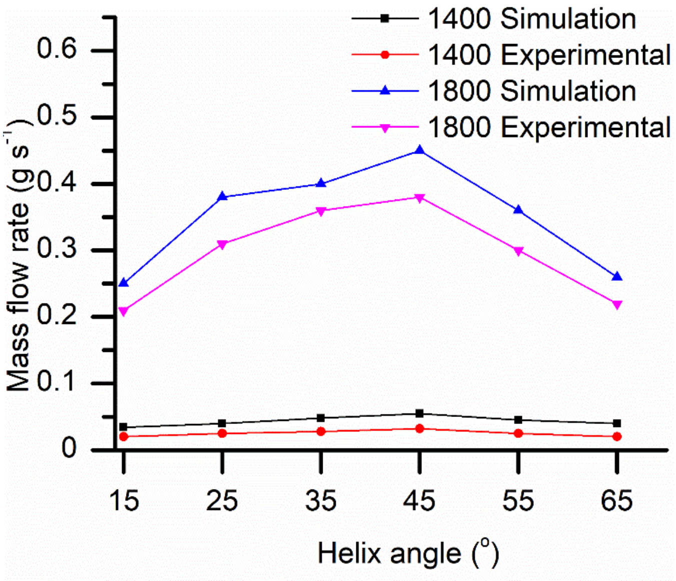

Figure 3.7 CFD validation with experimental results at 1400 rpm and 1800 rpm rotational speed

Among all the pumps, the 45° helix angle showed the highest mass flow rate of the lubrication oil (Figure 3.7). This can be explained by the concept of fluid path length and centrifugal force phenomenon. It is obvious from

Figure 3.3 Helical flutes of unibody axial flow pump

. that a 15° helix angle has a longer fluid path and higher centrifugal force as compared to a 65° helix angle where the fluid path is shorter, and the centrifugal force is lower. When the fluid path increases, the pressure losses increase, and vice versa. In the case of a 45° helix angle, the pressure losses and centrifugal force become optimum which leads to a higher mass flow rate. The effect of the helix angle on the pressure losses was also investigated and observed by Ozsipahi et. al. [53].

Therefore, the pump with a 45° helix angle was also experimentally tested at 2000, 2500, and 3000 rpm, and the simulation results were found to be in close agreement with the experimental results. Figure 3.8 shows the link between the experimental and numerical results of the average mass flow rate for the 45° helix angle pump in the range between 1400 and 3000 rpm.

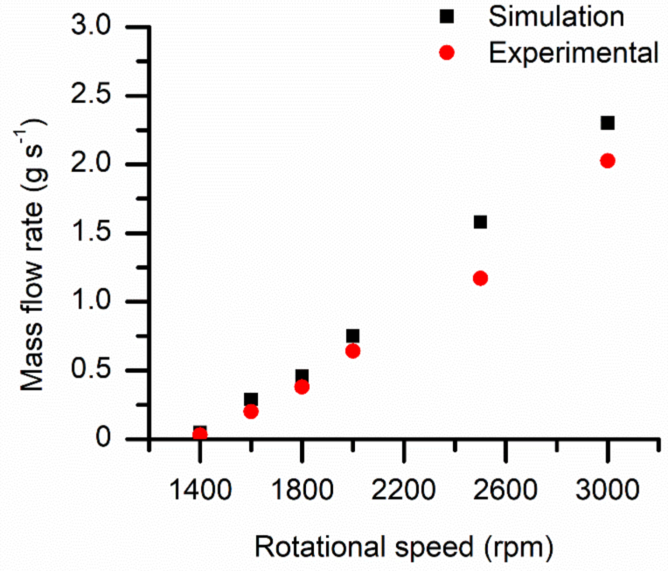

Figure 3.8 Mass flow rate of 45° helix angle pump at different rotational speeds

Results show a continuous increase in terms of mass flow rate by increasing the rotational speed. The mean absolute percentage error (MAPE) between the experimental and simulation results for the 45° helix angle pump at various speeds is shown in Table 3.2.

Table 3.2 Mean absolute percentage error (MAPE) of 45° helix angle pump

N (rpm)	Experimental (g s^{-1})	Simulation (g s^{-1})	Error (%)
1400	0.036	0.04	11.1
1800	0.38	0.45	18.4
2000	0.64	0.75	17.2
2500	1.16	1.5	29.3
3000	2.02	2.35	16.3

The maximum error between simulation and experimental results were found to be less than 30% which is comparable with the study of [54]. One of the important parameters in the lubrication system of a hermetic reciprocating compressor is the climbing time of the lubrication oil at the startup and it was observed to be 1 s at 1400 rpm and 0.4 s at 2000 rpm. Moreover, continuous flow of the lubrication oil from the outlet of the unibody axial pump was observed for rotational speeds greater than 1400 rpm. However, the pump was unable to raise the lubrication oil at speeds below 1400 rpm irrespective of the helix angle.

The lubrication oil was then heated to a temperature of 40°C and 60°C which corresponds to 7.5 cSt and 4.6 cSt viscosity respectively to explore the effect of viscosity on the mass flow rate of the lubrication oil. It was observed that the minimum rotational speed to raise the lubrication oil was still 1400 rpm. However, at rotational speeds greater than 1400 rpm, the mass flow rate was observed to be increased when the viscosity was decreased as shown in Figure 3.9.

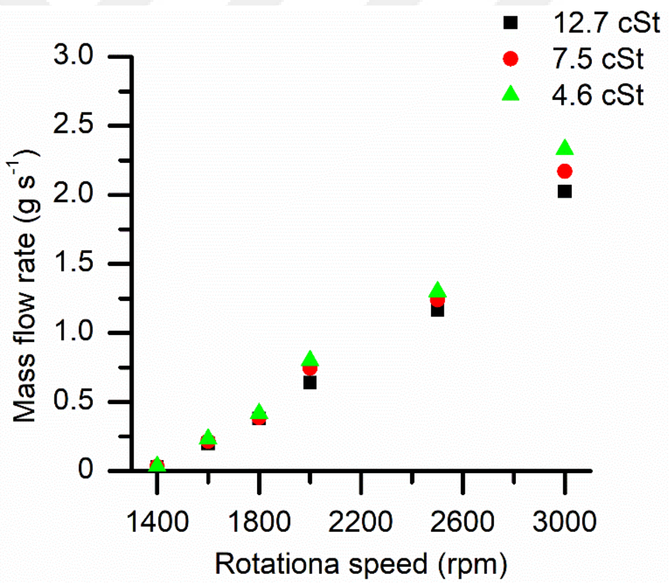

Figure 3.9 Experimental mass flow rate and viscosity of the lubrication oil

Such a relationship between viscosity and the mass flow rate was also observed in the study of Ozsipahi et.al. [54].

In addition, the Reynolds number based on the oil mass flow rate measured experimentally at 3000 rpm was calculated using Eq. (3.1) which shows the laminar flow assumption in the simulation was true.

$$Re = 4\frac{\dot{m}}{\pi \mu d_h} \cong 300 \tag{3.1}$$

3.5 Conclusion

The main aim of the study was to develop a lubrication oil pump system for inverter-type hermetic reciprocating compressors. The lubrication system was based on an additively manufactured unibody axial pump connected to the bottom of the crankshaft which was partially immersed in the lubrication oil sump. Six types of pumps were tested having helix angles of 15°, 25°, 35°,45°, 55°, and 65°. It was observed that the unibody axial flow pump with a 45° helix angle has the maximum mass flow rate comparatively. The results indicate that the pump has the potential to raise the lubrication oil to the outer helical channel of the crankshaft at a low speed i.e., 1400 rpm. The effect of viscosity (4.6, 7.5, and 12.7 cSt) on the mass flow rate was also investigated and it was found that viscosity and mass flow rate are inversely proportional. The climbing time was studied to be 1 s at 1400 rpm and 0.4 s at 2000 rpm. Moreover, the CFD simulation was also performed, and it was found that the results are in good agreement with the experimental tests. The mass flow rate of oil coming out of the pump outlet was studied as a validation parameter. Numerical simulation could be used as a reliable tool for further studies of this pump.

Chapter 4

NEGATIVE ADDITIVE MANUFACTURING

4.1 Introduction

Ceramics like alumina (Al_2O_3) have exquisite mechanical and physical properties such as excellent compressive strength, high elastic modulus, high corrosion resistance, and stability (thermal and chemical) at elevated temperatures [62,63]. These excellent characteristics distinguish them from the other two groups of materials: polymers and metals and make them appropriate for a vast range of applications such as aerospace, locomotive, biomedical, and electronics. However, as with all ceramics, the manufacturability of alumina is challenging due to its high melting point and low fracture toughness. Moreover, high porosity, geometrical distortion, and catastrophic failure in the final part are also associated problems with the manufacturing of alumina [64–67].

These problems can be solved by the incorporation of metallic particle densifiers into an alumina matrix forming a ceramic matrix composite material [68–70]. The inclusion of Al particles into the alumina ceramics enhances the overall properties of the part [71–73]. The secondary metal phase has superior thermal conductivity and better thermal shock resistance than monolithic alumina ceramics [74]. Since metal particles deform plastically and confound cracks propagation, they can boost brittle ceramic matrix toughness. [72,75–78]. These ceramic composites can be fabricated through a variety of practices such as spark plasma sintering, reactive sputtering, related deposition methods, hot pressing, hot extrusion, infiltration, squeeze casting [79], stir casting [80], and thermal spray processing. In earlier works on aluminum oxide-metal composite materials, various-sized metals such as Cr, Ti, Ni, Cu, Fe, and W have been reinforced into alumina and results showed significant improvement in toughness and ductility [81–83]. Fine aluminum particles have high yield and breaking strength and could act as a second phase to increase the fracture toughness and ductility of brittle alumina [84–91]. However, uniform diffusion of the reinforcement densifier particles throughout the ceramic matrix, high interaction, and wettability are challenging tasks [92,93]. Furthermore, the manufacturing of highly complex geometries and interconnected holes having excellent surface finish quality and dimensional precision has also gained the attention of researchers in the recent past [94,95].

Mechanical alloying is a solid-state powder technology that is used for the production of homogeneous materials from elemental powder mixtures [96]. It involves continuous welding, fracturing, and re-welding of powder particles in a high-energy ball mill [97]. The high-energy ball milling technique can decrease the particle size and promote bonding between elements that have low interaction and wettability. Consistent dispersion of the fine metallic reinforcements and fine grain size of the ceramic matrix improve the mechanical properties of the composite. Moreover, the mechanical properties of the cermet have a tendency to enhance with increasing volume fraction and decreasing particle size of the reinforcement [98].

The introduction of Additive manufacturing (AM) into the manufacturing of ceramics presents completely new opportunities for tackling the above-mentioned challenges [99]. Adabptable manufacturing of highly complex structures with good surface finish and precision could be possible by AM manufacturing technique. Based on the feedstock, AM technologies can be categorized into slurry-based, powder-based, and bulk solid-based methods. Slurry-based 3D printing technologies such as Direct Ink Writing (DIW) have liquid solution dispersed with solid loading particles as feedstock. Direct Ink Writing (DIW) is an economical and relatively speedy manufacturing process compared with other 3D printing techniques [100]. The use of non-Newtanion fluid or slurries in DIW allows for shape and structure retention owing to the high solid loading and viscoelastic properties [101,102]. Therefore, this technique can be used to create a great range of various monolithic and cermet structures. [103–105]. The shape retention of the deposited part is governed by the yield shear stress of the slurry [106]. Nevertheless, higher solid loadings lead to several challenges such as air trapping and clogging of the nozzle. A negative additive manufacturing technique could solve these problems by using low-yield shear stress slurries [107–113]. The negative additive manufacturing technique integrates slurry casting with 3D printed sacrificial polymer mold. The complexity of the desired ceramic part depends on the mold design. However, the fabrication of the complete mold and the casting of the slurry into the mold may lead to voids in the green body because of high viscosity of the printing inks which leads to poor flow inside the mold [114,115]. The formation of these voids may be eliminated by the multi-material extrusion approach where the printable ink is cast into the polymer mold as the mold is built up layer by layer simultaneously [116]. The technique couples a conventional thermoplastic deposition head with a DIW deposition head. The conventional thermoplastic deposition head is widely used in additive manufacturing and provides excellent shape retention; therefore, it is used as a secondary deposition head to create a mold for the slurry deposited using the DIW head. In the literature, there are only a few studies available on negative additive manufacturing where researchers employed this technique for the manufacturing of using materials such as carbides [117] and hydroxyapatite [118], but there is no study on alumina-aluminum cermet material.

In this paper, a novel negative additive manufacturing by fused deposition technique is proposed to manufacture cermet (alumina reinforced with Al particle densifiers) parts having excellent geometrical accuracy, low porosity, and high density.

4.1 Materials and Methods

4.1.1 Materials

The materials used in this study were deionized (DI) water, sodium carboxymethylcellulose (CMC) binder with an average molecular weight of ~250,000 (Product# 419281, Sigma-Aldrich), α-Alumina (Al_2O_3) powder (Nanokar, Turkey, 99.9% purity) with mean particle size provided in the datasheet from the manufacturer is of 35-40 μm and density of 3.97 g/cm^3 and aluminum (Al) powder particles (Nanokar, Turkey, 99.9% purity) with average particle size 5-10 μm. Since Al is highly reactive with DI water producing hydrogen gas and causing foaming problems, Sodium silicate (Sinopharm Chemical Reagent Co., Ltd., Shanghai, China) was used as a hydrogen inhibitor. The detailed experimental procedure used herein is shown in Figure 4.1.

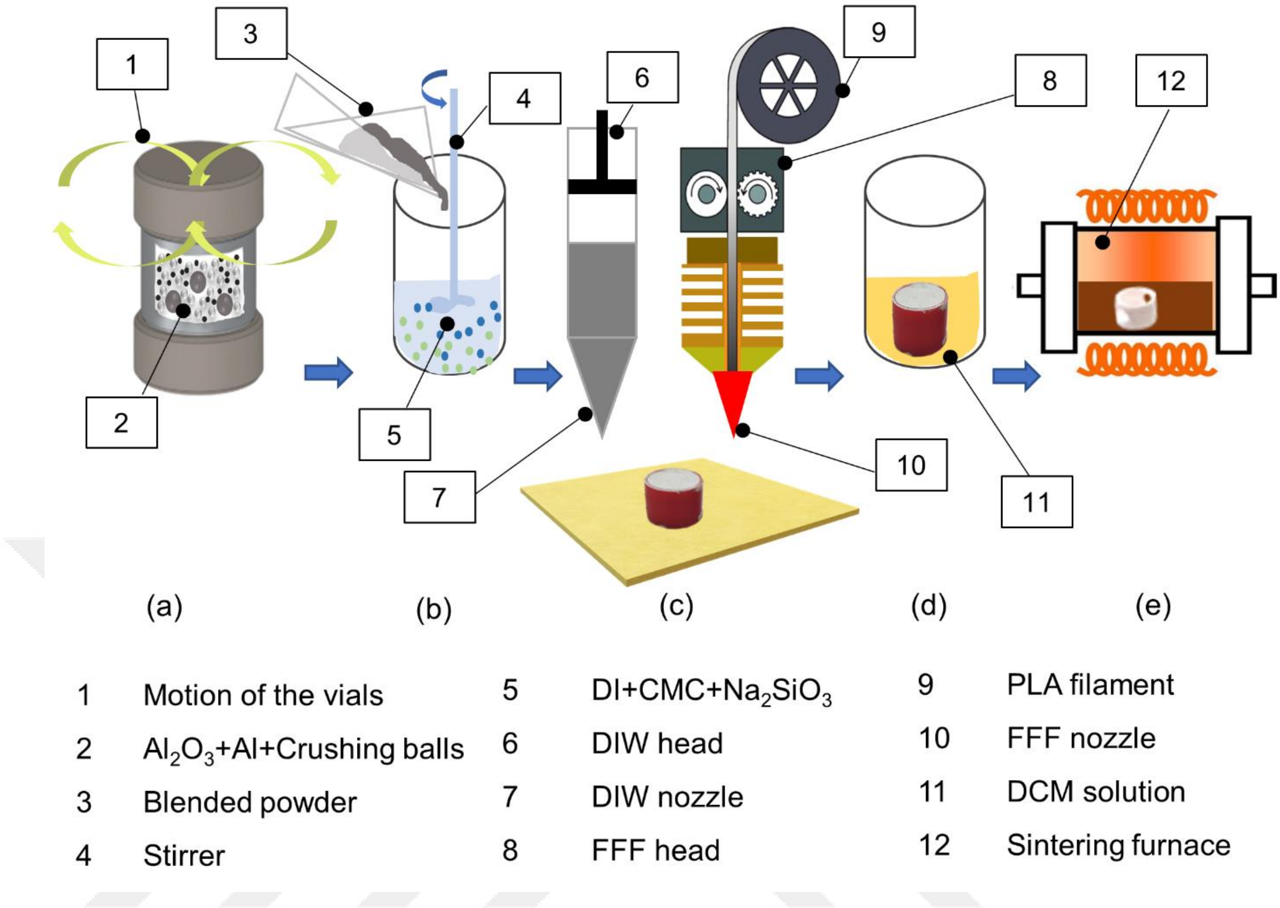

Figure 4.1 Graphical chart of the experiment. (a) High energy ball milling (b) Slurry (a) Negative Additive Manufacturing by Direct Ink Writing (DIW) (d) Demolding (e) Sintering in Argon gas environment at 1400°C

To achieve homogenous blended mixtures of alumina and aluminum (5 vol.%, 10 vol.%, 15 vol.%, 20 vol.%), raw powders were processed for one hour in SPEX TM SamplePrep 8000D Dual Mixer/Mill having two stainless steel vials. The rotational speed of the mill disc was set to the 1200 rpm value. Powders were weighed and mixed for a typical charge of 7g and three aluminum oxide balls with a 12 mm diameter for each vial. The ball-to-powder weight ratio (BPR) was about 5:1. The charging of powders was carried out under an argon atmosphere and kept hermetically sealed during the milling operation to avoid oxidation of Al particles. To prevent cold welding of powder particles between themselves (formation of agglomeration), onto the internal surfaces of the chamber of the mill and to the surfaces of the grinding medium during milling, 1 ml stearic acid was used as the process control agent (PCA). The cooling time after every 10 minutes of milling was 2 minutes.

4.1.2 Slurry preparation and rheology

The milled powder was filtered to eliminate large agglomerates. A feedstock solution was then prepared by stirring carboxymethyl cellulose (CMC) binder into a flask of deionized water until a 25 wt.% solution was obtained. The solution was then mixed in a mechanical mixer to achieve a smooth and homogenous slurry. The prepared solution was then kept in a refrigerator at 4°C for 2 hours, allowing bubbles to dissipate. The milled powder was then added to this stock solution in a step-by-step approach to prepare a slurry containing various Al compositions. Since Al is highly reactive with water, producing hydrogen gas, 1 wt.% sodium silicate was added as a hydrogen inhibitor. The slurry was then defoamed and loaded into a 200 mL pneumatic dispenser. This was done by scooping the slurry out of the jar with a flat spatula and smearing it over the top opening of the dispenser, being cautious to make sure no air bubbles get caught between consecutive scoops. The rheology of the cermet slurry was analyzed from 0.1 s^{-1} to 1000 s^{-1} at 20 ˚C on a Malvern Kineus pro rheometer. A parallel plate geometry of 25 mm diameter with a compatible solvent trap was used at a gap of 0.3 mm.

4.1.3 Negative additive manufacturing

A multi-material robotic additive manufacturing setup comprising a Fused Filament Fabrication (FFF) tool-head and a Direct Ink Writing (DIW) tool-head was employed for the negative additive manufacturing of samples. The FFF tool-head deposits the thermoplastic polymer polylactic acid (PLA) using a motorized extruder with a 0.4 mm nozzle. The DIW tool-head deposited the Al_2O_3-Al slurry using a pneumatic extruder with a nozzle of 0.4 mm. The inlet pressure of the pneumatic extruder was regulated using a pressure regulator. Both of the tool-heads were mounted on a robotic arm in the elbow-up posture. The multi-material robotic additive manufacturing setup is illustrated in Figure 4.2.

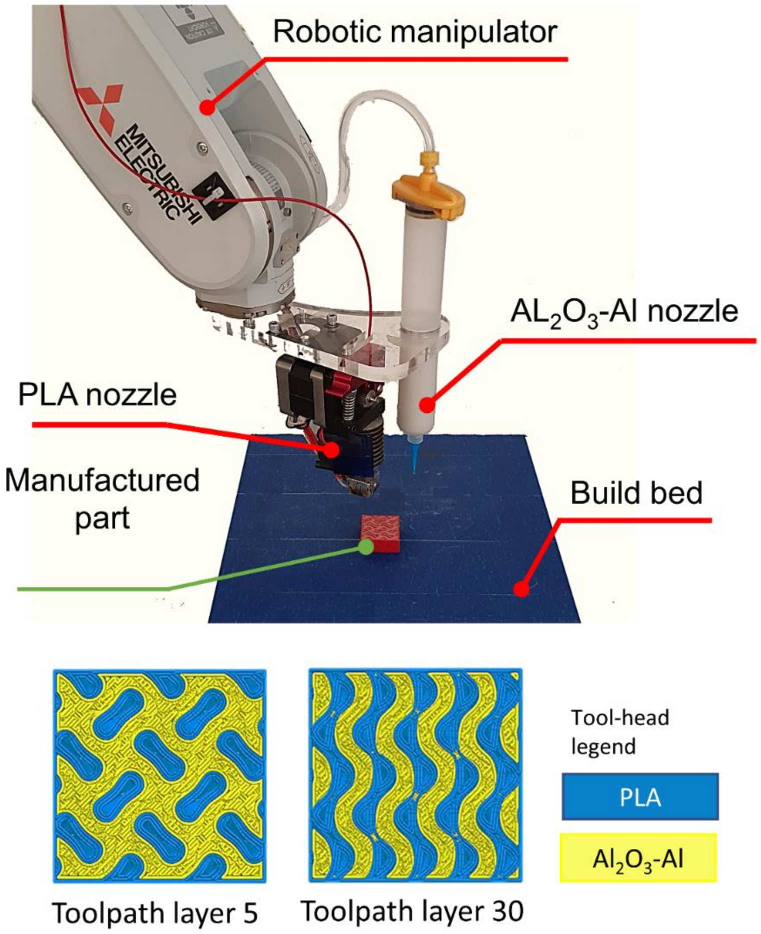

Figure 4.2 FFF and DIW heads on a robotic arm along with the tool path of two distinct layers

The toolpath for the multi-material AM is generated using the process parameters tabulated in Table 4.1 using the Ultimaker Cura software in the dual nozzle offset compensation mode. The toolpath was then post-processed for the robot's controller using a customized MATLAB script. One layer of the PLA mold was fabricated first, and the corresponding layer of Al_2O_3-Al slurry was then deposited inside the mold immediately. The toolpath of two distinct layers is illustrated in Figure 4.2 where the difference in the tool path of the PLA and Al_2O_3-Al slurry is indicated.

Table 4.1 Printing parameters for the multi-material DIW

Parameter	FFF Head	DIW Head
Nozzle diameter	0.4 mm	0.4mm
Material	PLA	Cermet (Alumina-Al)
Build temperature	200°C	20°C
Layer height	0.2 mm	0.2 mm
Extrusion width	0.4 mm	0.4 mm
Linear speed	20 mm.s^{-1}	10 mm.s^{-1}
Infill pattern	Rectilinear	Rectilinear
Infill density	0%	100%
Shell	2	2
Air Pressure	-	0.2 Mpa

4.1.4 Drying, demolding, and sintering

Drying of the printed parts was carried out at room temperature for 24 hours. The dried parts were then submerged in Dichloromethane (DCM) for demolding. DCM quickly dissolved PLA mold leaving behind the cermet green body. DCM is insoluble and perfectly inert to the CMC binder material; therefore, the part didn't break or deform during the demolding process. The CAD geometry of the molds and demolded parts is shown in Figure 4.3.

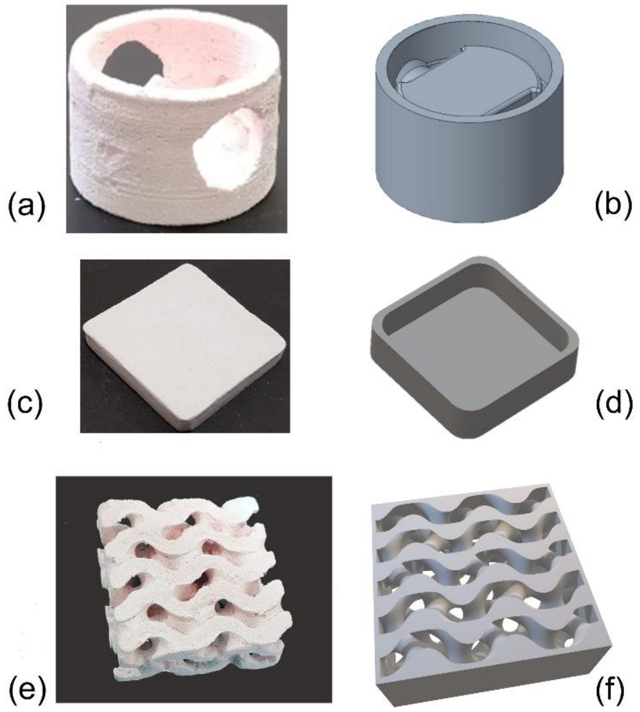

Figure 4.3 (a) Demolded piston part (b) piston mold (c) demolded cube part (d) cube mold (e) demolded complex gyroid part (f) complex gyroid mold

For the pressure-less sintering of cermet green parts, a multi-stage heating regime was implemented inside a chamber furnace. The multi-stage sintering regime is demonstrated in Figure 4.4.

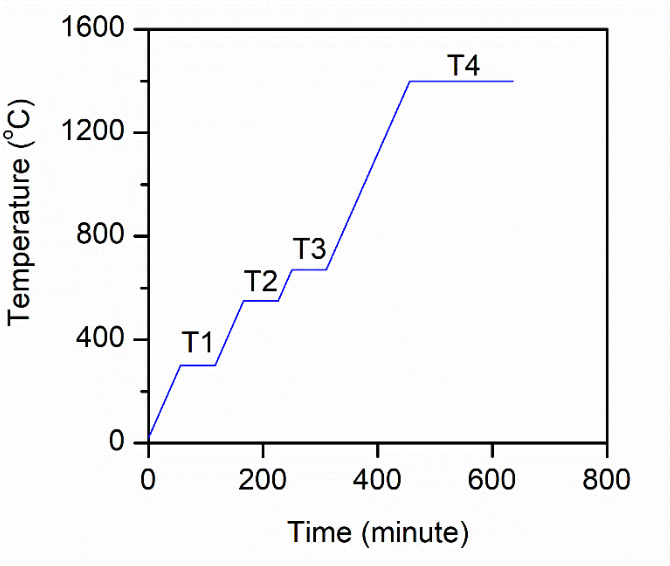

Figure 4.4 The multi-stage sintering regime for the sintering of cermet green parts

All heating rates were 5°C min^{-1}. The sintering process was carried out under an Argon gas atmosphere. First, the furnace was heated from room temperature to 300°C (T1) followed by an isothermal hold of 60 minutes to burn out the CMC binder. Next, the furnace was heated to 500°C (T2) followed by an isothermal hold of 30 minutes to burn away any PLA traces that were left behind during the demolding process. Then, the furnace was heated to 670°C (T3) followed by 60 minutes of isothermal hold for melting and diffusion of Al particles into the alumina ceramic matrix. In the final step, the furnace was heated to 1400°C (T4) followed by an isothermal hold of 3 h to sinter the cermet green body. The sintered samples were taken out from the furnace after the temperature of the furnace dropped down to room temperature. The parts exhibited geometrical and dimensional accuracy.

4.1.5 Characterization

The theoretical densities of the cermet parts were calculated using the rule of mixture. After sintering, bulk density and the porosity of the printed parts were measured according to ATM C830-00, by the Archimedes method.

The microhardness of the specimen was measured according to ASTM C 1327-03, with a Vickers hardness tester (HMV-G Series microhardness tester,). A load of 0.98 N was applied using a diamond indenter for a time of 10 seconds. Indent sizes were measured by optical microscopy. The hardness values of were measured as an average of 10 readings along the specimen cross-section surface.

To examine the impact of ball milling on the morphology and homogeneity of the cermet mixture, scanning electron microscope (SEM) was performed.

X-ray diffraction (XRD) analysis of the milled powder and sintered part was carried out by X-ray diffractometer using Cu Kα radiation with a wavelength of 0.154 nm at 45kV and 40 mA current. The XRD peaks were recorded in the 2θ range between 20° and 90°. The peaks were analyzed using the standard procedure to see the phases.

4.2 Results and discussion

4.2.1 SEM and XRD analysis

Figure 4.5 shows SEM and EDX mapping images of Al_2O_3-20 vol.% Al cermet powders after one hour of high-energy ball milling. Fine crystallites were produced from the initial micrometer-sized powder by performing the high energy ball milling operation. The milled powder consists of agglomerates. During the high-energy ball milling, relatively soft aluminum particles underwent a significant plastic deformation while the alumina brittle particles also fragmented leading to uniformly dispersed powder particles exhibiting homogenous size distribution (Fig. 4.5 (a) and (b)). The FE-SEM images of the sample revealed the existence of a composite structure. These images (Fig. 4.5 (c) and (d)) consist of different regions corresponding to the Al_2O_3 matrix and Al reinforcement particles. Here, while the reinforcement particles are homogenously dispersed, the matrix phase existed in larger grains. Thus, no reaction takes place between the reinforcement and matrix phases. This is also supported by the EDX mapping analyses (Fig. 4.5 (e), (f), and (g)), which revealed the Al and O elements together. In addition, the EDX spectrum (Fig. 4.5 (h)) clearly showed that there is no impurity element in the structure. The carbon peak between 0.2-0.3 keV is due to the sample holder. Based on microscopic analysis, the mechanism explanation for the effect of aluminum on the properties of alumina-based ceramics can also be explained. As clearly observed, aluminum is well dispersed in the matrix forming a homogenous and dense microstructure. Since the melting temperature of aluminum is relatively low (660°C), during the third stage of sintering, where the temperature was kept constant at 670°C for one hour, the aluminum melted and flew through the porous structure of alumina thus leading to higher densification.

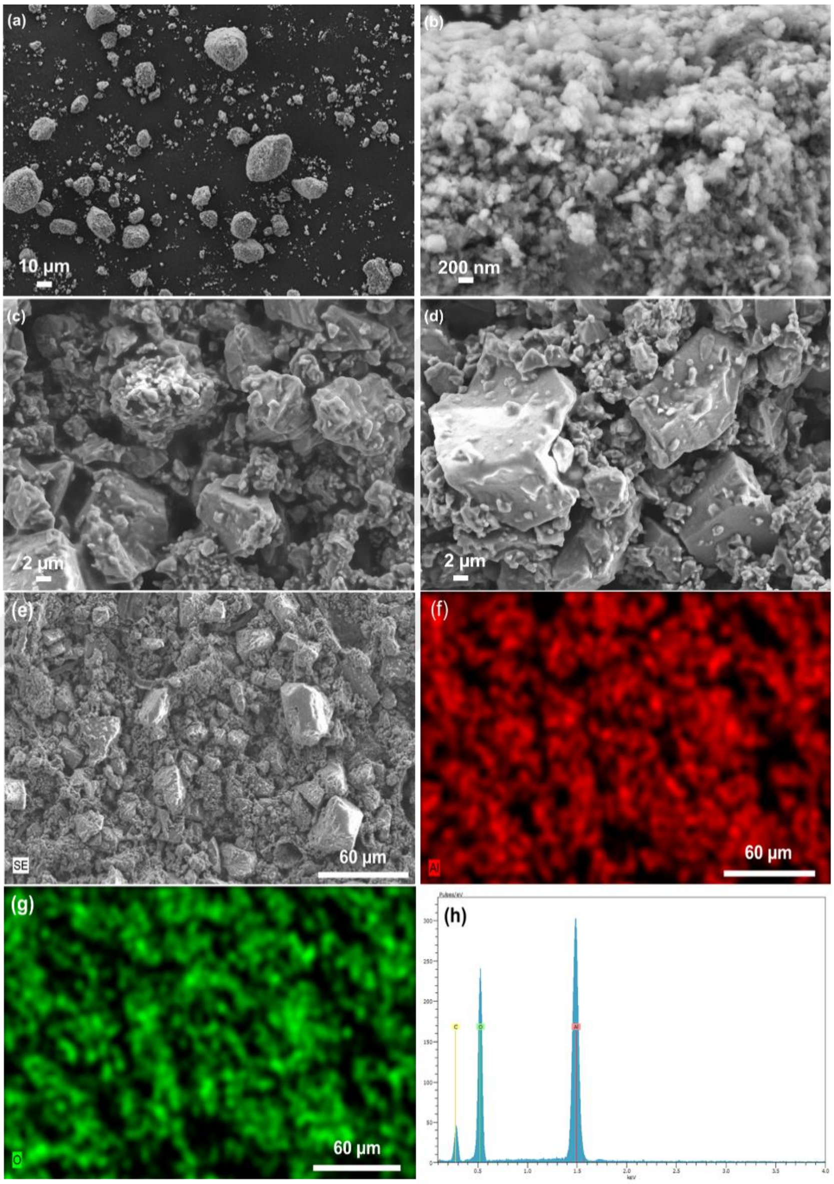

Figure 4.5 Secondary electron FE-SEM images of milled Al2O3-20 vol.% Al powder (a, b, c, d), SEM image of milled Al_2O_3-20 vol.% Al powder (e), EDX mapping of Al (f), O (g), and EDX spectrum (h).

The X-ray Diffraction (XRD) patterns of as-milled Al_2O_3-20 vol.% Al powder are shown in Figure 4.6.

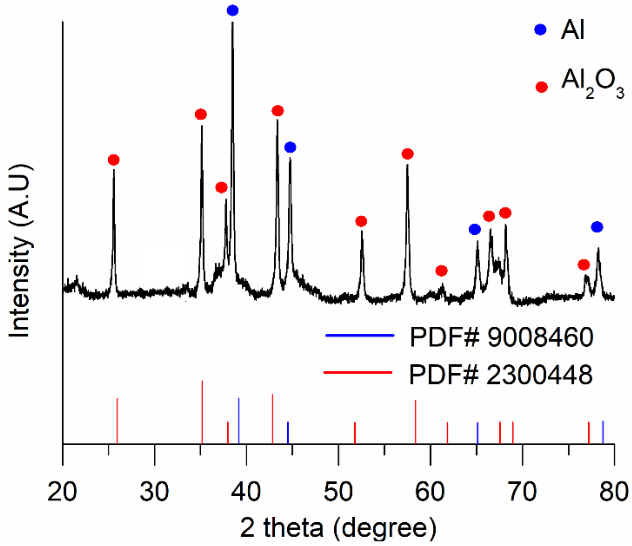

Figure 4.6 XRD plot of Al_2O_3-20 vol.% Al cermet milled powder

It is obvious that only two phases of alumina and aluminum were found in the as-milled powder. This is mainly because of Argon environment milling. Al is reactive in the open air and could form aluminum oxide if the milling is carried out in atmospheric conditions. Furthermore, the sintered parts were also characterized by phases. Figure 4.7 shows the XRD peaks for the sintered part which mainly consists of Al_2O_3-20 vol.% Al solid loading.

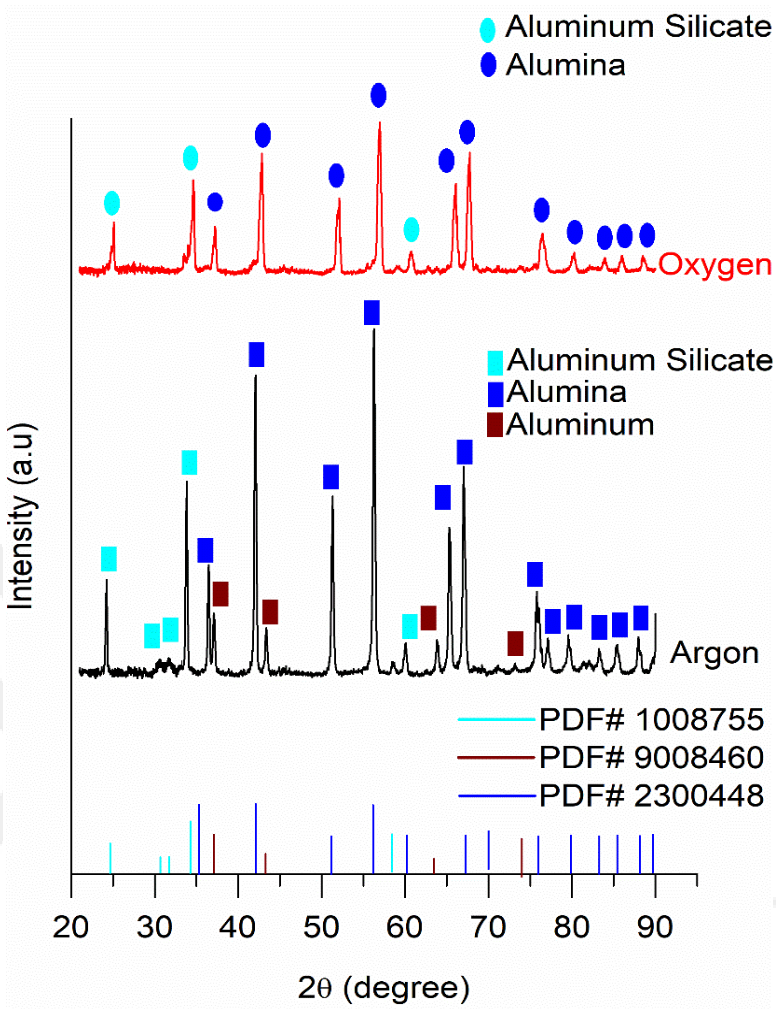

Figure 4.7 XRD plot of Al_2O_3-20 vol.% Al cermet sintered part

When the parts were sintered under atmospheric conditions, all the Al was converted into aluminum oxide hence there were no Al peaks observed. However, when the parts were sintered under Argon conditions, the Al was present as a distinct phase. Aluminum Silicate peaks can be seen in the XRD results. This is because of 1 wt. %sodium silicate addition in the slurry for hydrogen inhibition. Slurries without sodium silicate exhibit the foaming problem which can be seen in Figure 4.8.

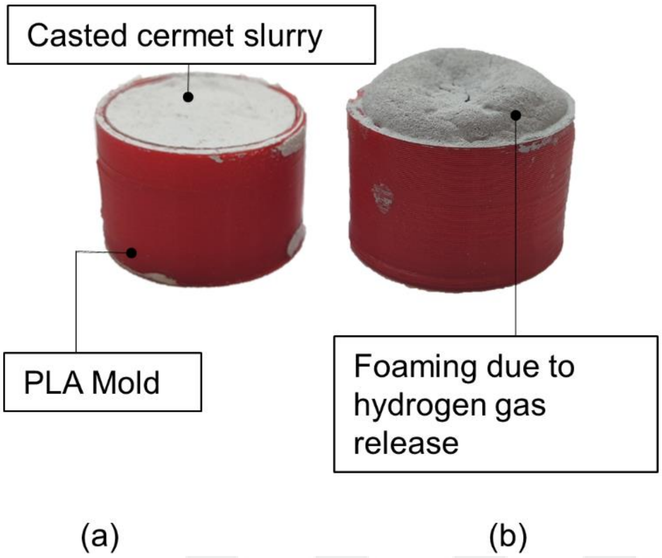

Figure 4.8 Negative additive manufactured part (a) showing no hydrogen production in the presence of 1 wt. % sodium silicate (b) Foaming due to the hydrogen production in the absence of hydrogen inhibitor

Aluminum powder can react with deionized water to produce hydrogen gas [119]. Sodium silicate was used to inhibit hydrogen production. A protective layer of silicon formed on the Al particles, which prevented them from reacting with deionized water to produce hydrogen. This phenomenon was also studied by Xin Zhen et al. [120].

4.2.2 Rheology analysis

The rheology of the slurry plays an important role in finding its suitability in the Direct Ink Writing (DIW) technique. The increase in viscosity and shear stress against shear rate was measured. Figure 4.9 shows viscosity and shear stress as a function of shear rate for four types of slurries (Al_2O_3-5vol.% Al, Al_2O_3-10vol.% Al, Al_2O_3-15vol.% Al, Al_2O_3-20vol.% Al).

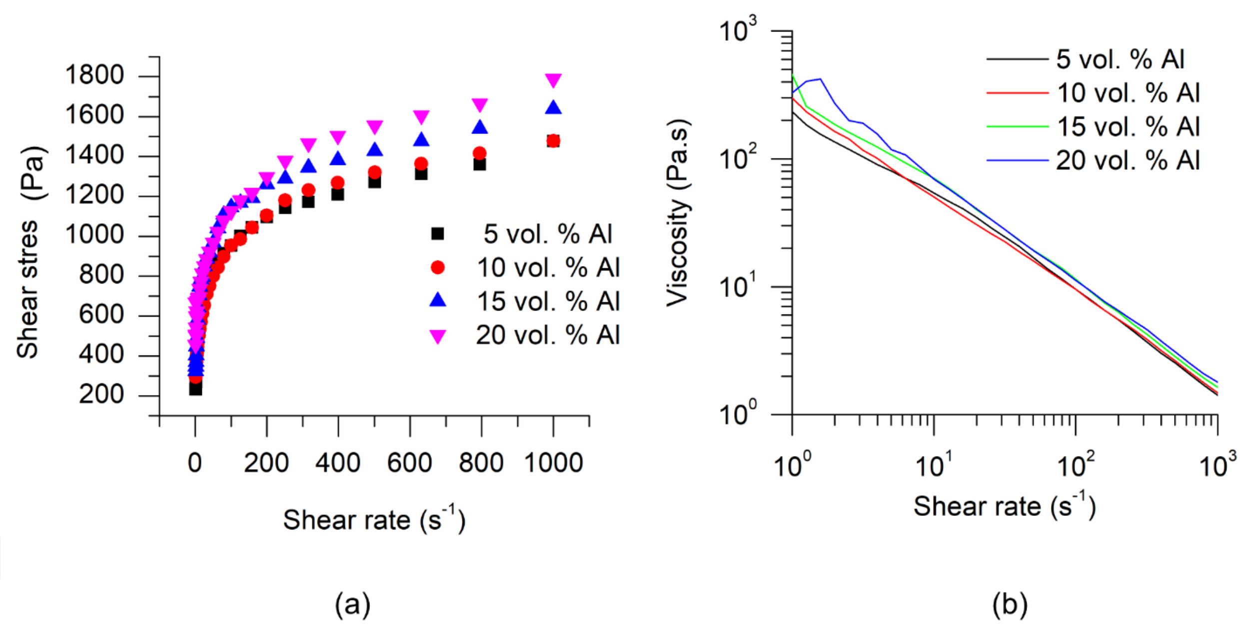

Figure 4.9 Rheology analysis of the slurries containing various amounts of Al (a) Shear stress vs shear rate (b) Viscosity vs shear rate

The slurries demonstrated a non-Newtonian shear thinning behavior that can be modeled using the Herschel–Bulkley model which can be represented mathematically as

$$\tau = \tau_o + k\dot{\gamma}^n \tag{4.1}$$

where τ is the shear stress [Pa], τ_o is the yield shear stress [Pa], k is the consistency factor [Pa.s^n], $\dot{\gamma}$ is the stress rate [s^{-1}], and n is the flow index [dimensionless]. The consistency factor and flow index of the slurries are tabulated in Table 4.2.

Table 4.2 Herschel-Bulkley parameters for the four different slurries

Slurry	τ_o [Pa]	k [Pa.s^n]	n
5 vol% Al	270	313	0.22
10 vol% Al	280	441	0.19
15 vol% Al	295	343	0.20
20 vol% Al	300	331	0.20

It was found that the viscosity of the slurry slightly increases with the addition of Al content keeping the solid loading constant. However, this can be concluded that the Al content does not affect the viscosity of the slurry a great deal. On the other hand, the shear stresses of the slurry increase as the Al content increases keeping the overall solid loading constant. Such an increase in the shear stress can be ascribed to the Al particle-CMC binder interfaces in the slurry. As the amount of Al increases, the number of Al-CMC interactions increases. Nevertheless, all the slurries exhibited yield shear stress greater than zero and were shear thinning at stresses above the yield stress. The non-Newtonian behavior of the solution of CMC which is mainly attributed to the disentanglement of CMC chains is retained in the slurry [121].

The shear rate during DIW with a nozzle of circular exit cross-section is defined as

$$\dot{\gamma} = \frac{4Q}{\pi r^3} \tag{4.2}$$

where, $\dot{\gamma}$ is the shear rate [s^{-1}], Q is the volumetric flow rate [$mm^3.s^{-1}$], and r is the radius of the nozzle [mm]. The shear rate during the DIW of the slurries was calculated as 194 s^{-1} which corresponds to a viscosity in the range of 5 – 7 Pa.s for all four types of slurries. Such a low level of viscosity facilitates the flow through the fine nozzle without clogging during the DIW process. Once the slurry is deposited, the viscosity of the material increases by two orders of magnitude. However, the deposited slurry will not be able to retain its shape since the yield shear stress of the slurries is too low. Therefore, the PLA mold is necessary for additive manufacturing using these slurries.

4.2.3 Density and micro-hardness

The relative densities of the cermet Al_2O_3-Al parts attained by pressure-less sintering are given in Figure 4.10. The true volume of the sintered part was measured using the Archimedes immersion technique and the pore volume was measured by the water retention technique.

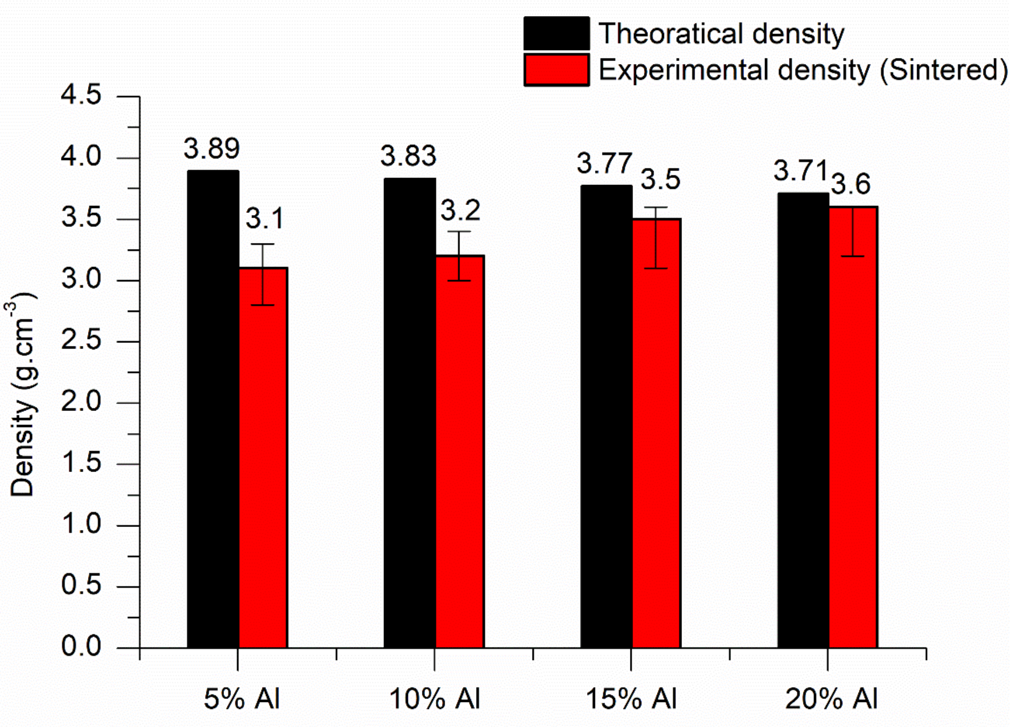

Figure 4.10 Densities of sintered (1400°C) parts having the various amount of Al content

It is obvious that the aluminum content is directly related to the densities of the Al_2O_3-Al cermet parts. The highes density achieved was 97.03% corresponding to 20 vol.% Al. This can be explained by the melting of the Al metal particles which enhanced the wettability of Al_2O_3 ceramic particles thus accelerating the diffusion process.

Figure 4.11 shows the Vickers micro-hardness test results. Processing conditions, porosity, and the degree of densification are the governing parameters that define the micro-hardness of the ceramic part. It is obvious that the micro-hardness of the sintered Al_2O_3-Al cermet part decreases upon the addition of Al metal particles. It varies from 1650 HV for 5 vol.% aluminum to 1430 HV for the cermet material with 20 vol.% Al. There are two reasons behind this phenomenon: 1) Low fraction of the hard ceramic phase and mutual sliding of ceramic grains and 2) the plastic flow of the soft metal phase Al under the Vickers indenter loading.

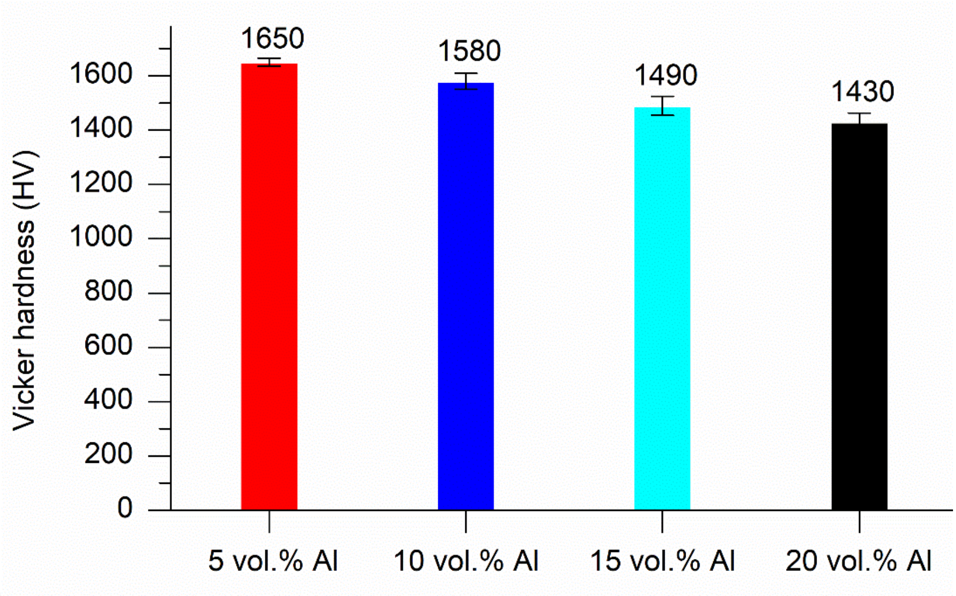

Figure 4.11 Vickers micro-hardness for the sintered Al2O3-Al cermet parts with various Al content

The parts of simple and complex geometries produced by the negative additive manufacturing technique using multi-material extrusion demonstrate the efficacy of the technique to produce parts from low-yield shear stress slurries. The multi-material extrusion combined DIW to FFF and help the part retain its shape which otherwise is achievable by the DIW method for low yield shear strength slurries. The developed method can be used to additively manufacture using slurries of other ceramics and ceramets.

4.3 Conclusion

A multi-material Direct Ink Writing (DIW) approach that involves the layer-by-layer manufacturing of PLA mold and Al_2O_3-Al cermet material simultaneously is presented. A homogenous cermet mixture in the form of Al_2O_3-Al with various Al compositions (5 vol.%, 10 vol.%, 15 vol.%, and 20. vol%) was achieved by high-energy ball milling. Slurries were prepared using these powders by mixing the CMC, and sodium silicate in deionized water. The negative additive manufacturing approach has been successfully used to print simple three-dimensional parts along with a piston for the hermetic reciprocating compressor. It can be concluded that it is possible to formulate printable alumina-aluminum cermet slurries exhibiting shear thinning behavior with solid contents as high as 50 vol.% that reached densities up to 97% after sintering.

Chapter 5

CONCLUSION

5.1 Overview

A brief overview of the tasks which were performed during the present research work and the main conclusions are given below.

- An innovative approach to design, manufacture, and test a novel unibody axial flow oil pump for a hermetic reciprocating compressor has been developed. The 3D-printed unibody axial pump is capable to supply lubrication oil to all bearings of the compressor at a wide range (1400 – 5000 rpm) of speed. Six types of pumps were tested having helix angles of 15°, 25°, 35°,45°, 55°, and 65°. It was observed that the pump with a 45° helix angle has the maximum oil mass flow rate comparatively. The results imply that the pump has the potential to raise the lubrication oil to the outer helical channel of the crankshaft at a low speed i.e., 1400 rpm. The effect of viscosity (4.6, 7.5, and 12.7 cSt and it was found that viscosity and mass flow rate are inversely proportional. Furthermore, the CFD simulation was also performed, and it was found that the results are in good agreement with the experimental tests. Numerical simulation could be used as a reliable tool for further studies of this pump.
- Laser surface texturing was successfully applied to the piston of a hermetic reciprocating compressor by using Micro-Fab laser equipment. Four types of textures were introduced and characterized in terms of coefficient of

performance. Continuous radial, axial, and mesh grooves led to a lower COP. It was realized that the continuous groove pattern suppressed the hydrodynamic pressure. However, the micro-dimple pattern texture led to a higher COP as compared to the baseline untextured piston. Furthermore, the textured piston has a significant effect on the gas leakage from the piston cylinder clearance. In addition, the cooling capacity of the compressor having a micro-dimpled piston was found to be increased by 1 W as compared with the non-textured piston hermetic compressor.

- This thesis also demonstrates the potential of negative additive manufacturing using cermet materials (Al_2O_3-Al). The MARC multi-material Mitsubishi robotic additive manufacturing setup is capable of printing different types of material in a single build. A multi-material additive manufacturing approach is presented that involves the layer-by-layer manufacturing of PLA molds. The cermet material paste is cast into the molds gradually as the PLA layers are built. The PLA mold improves the shape retention of the cermet slurry. The additively manufactured cermet green body is demolded by dissolving the PLA mold in an organic solvent (DCM). A homogenous cermet mixture in the form of Al_2O_3-Al with various Al compositions (5 vol%, 10 vol%, 15 vol%, and 20. vol%) was achieved by high-energy ball milling. All the slurries were made using these powders by mixing the CMC binder, and sodium silicate (hydrogen inhibitor) in DI water. The negative additive manufacturing approach has been successfully used to print various parts along with a piston for the hermetic reciprocating compressor. It can be concluded that it is possible to formulate printable alumina-aluminum cermet slurries exhibiting shear thinning behavior with solid contents as high as 50 vol% that reached densities up to 97% after sintering. The piston manufactured from the cermet material was found to be 10 times lighter in weight as compared to the existing piston of the hermetic reciprocating compressor.

5.2 Recommendations for future work

Although the unibody axial flow pump is able to solve the lubrication problem at a low speed of 1400 rpm, further work still needs to be done to reduce the minimum working speed to 900 rpm as this is the lowest speed for an inverter-type hermetic reciprocating compressor at which the mechanical losses are at a minimum. Furthermore, this pump could be directly integrated with the crankshaft as a single body and its efficiency could be studied.

Micro-texture on the piston shows good results in terms of the coefficient of performance of the compressor. Such micro-texture could be studied further on the crankshaft bearing too. Moreover, the texture produced by other ways such as micro-milling, micromechanical texturing, shot blasting, diamond embossing, micro-casting, reactive ion etching, and pulsed air arc treatment could also be explored in this field.

Designing a correct viscoplastic slurry that can flow easily under shear stress and rapidly recover and retain its shape upon deposition is one of the problems associated with Direct Ink Writing technique. Other than exhibiting the right and appropriate rheology, high solid loading is also the most preferable parameter while designing the paste. Increasing the solid loadings will not only reduce the shrinkage in the final part but high density can also be achieved. Sometimes it is very hard to prepare slurry which has the right rheology and therefore to print parts from a such paste that do not collapse and hold their shape after deposition. In such cases, polymer curing can be done to fabricate parts with minimum distortion. The designing slurry which can flow through extremely fine nozzles (< 1 mm) to produce small parts with exceptionally fine details is another challenge to tackle with. Using nano-sized powder particles with appropriate additives might be one way to achieve this task. Air trapping is another challenge that needs to be solved when manufacturing bulk materials that need the piling of many layers. One way to solve this issue is to use the correct overlap degree between each layer and thus lower the height between them to slightly deform the filament during the DIW process to fill the empty spaces. In certain instances, cold/hot isostatic pressing, or lamination is applied after printing to remove the trapped gases but, such post-processing treatments influence the microstructure of the finished part. One of the critical and most important challenges in Direct Ink Writing methodology is to manufacture large overhangs or spans with perfect geometrical accuracy despite using slurry with optimized rheology. To address this issue, researchers are using sacrificial supports to grow the range of geometries that can be manufactured by the DIW. Printing of sizable parts with very delicate features needs infinitesimal nozzles which means the printing time will be significantly large.

Although DIW is an eco-friendly process that can be used to fabricate products on request without mold or machining processes, post-printing processes such as sintering require a lot of energy. It is essential to build a methodology by which post-printing procedures can be minimized. Field-assisted sintering technique or cold sintering method can be made more effective or they can be integrated into the printing process in a single step.

BIBLIOGRAPHY

[1] Kerpicci H, Sahin C, Ozdemir AR. A New Approach to Mechanical Loss Measurement of a Reciprocating Compressor. IOP Conf. Ser. Mater. Sci. Eng., vol. 604, IOP Publishing; 2019, p. 12057.

[2] Yang B, Ziviani D, Groll EA. Comprehensive model of a hermetic reciprocating compressor. IOP Conf. Ser. Mater. Sci. Eng., vol. 232, IOP Publishing; 2017, p. 12007.

[3] Xiao S, Xiao Q, Song M, Zhang Z. Dynamic Analysis for a Reciprocating Compressor System with Clearance Fault. Appl Sci 2021;11:11295.

[4] Dumitru G, Romano V, Weber HP, Haefke H, Gerbig Y, Pflüger E. Laser microstructuring of steel surfaces for tribological applications. Appl Phys A 2000;70:485–7.

[5] Ai X, Cheng HS. The effects of surface texture on EHL point contacts. Journal of Tribology 1996;118:59-66.

[6] Etsion I, Burstein L. A model for mechanical seals with regular microsurface structure. Tribol Trans 1996;39:677–83.

[7] Hamilton DB, Walowit JA, Allen CM. A theory of lubrication by microirregularities. Journal of Fluids Engineering 1966;88:177.

[8] Babu PV, Ismail S, Ben BS. Experimental and numerical studies of positive texture effect on friction reduction of sliding contact under mixed lubrication. Proc Inst Mech Eng Part J J Eng Tribol 2021;235:360–75.

[9] Mansouri SH, Wong VW. Effects of piston design parameters on piston secondary motion and skirt-liner friction. Proc Inst Mech Eng Part J J Eng Tribol

2005;219:435–49.

[10] Etsion I, Kligerman Y, Halperin G. Analytical and experimental investigation of laser-textured mechanical seal faces. Tribol Trans 1999;42:511–6.

[11] Ronen A, Etsion I, Kligerman Y. Friction-reducing surface-texturing in reciprocating automotive components. Tribol Trans 2001;44:359–66.

[12] Brizmer V, Kligerman Y, Etsion I. A laser surface textured parallel thrust bearing. Tribol Trans 2003;46:397–403.

[13] Kligerman Y, Etsion I, Shinkarenko A. Improving tribological performance of piston rings by partial surface texturing. J Trib 2005;127:632–8.

[14] Han J, Fang L, Sun J, Wang Y, Ge S, Zhu H. Hydrodynamic lubrication of surfaces with asymmetric microdimple. Tribol Trans 2011;54:607–15.

[15] Siripuram RB, Stephens LS. Effect of deterministic asperity geometry on hydrodynamic lubrication. J Trib 2004;126:527–34.

[16] Ramesh A, Akram W, Mishra SP, Cannon AH, Polycarpou AA, King WP. Friction characteristics of microtextured surfaces under mixed and hydrodynamic lubrication. Tribol Int 2013;57:170–6.

[17] Gadeschi GB, Backhaus K, Knoll G. Numerical analysis of laser-textured piston-rings in the hydrodynamic lubrication regime. J Tribol 2012;134:4.

[18] Tomanik E, Profito FJ, Zachariadis DC. Modelling the hydrodynamic support of cylinder bore and piston rings with laser textured surfaces. Tribol Int 2013;59:90–6.

[19] Vincent C, Monteil G, Barriere T, Gelin JC. Control of the quality of laser surface texturing. Microsyst Technol 2008;14:1553–7.

[20] Vilhena LM, Sedlaček M, Podgornik B, Vižintin J, Babnik A, Možina J. Surface texturing by pulsed Nd: YAG laser. Tribol Int 2009;42:1496–504.

[21] Ozu S, Umehara N, Sasaki S. Effect of pattering of steel slider on the friction properties sliding against cast iron plate under oil lubrication condition. Proc Asiat 2006:667–8.

[22] Bulatov VP, Krasny VA, Schneider YG. Basics of machining methods to yield wear-and fretting-resistive surfaces, having regular roughness patterns. Wear 1997;208:132–7.

[23] Greco A, Raphaelson S, Ehmann K, Wang QJ, Lin C. Surface texturing of tribological interfaces using the vibromechanical texturing method. J Manuf Sci Eng 2009;131:06.

[24] Wakuda M, Yamauchi Y, Kanzaki S, Yasuda Y. Effect of surface texturing on friction reduction between ceramic and steel materials under lubricated sliding contact. Wear 2003;254:356–63.

[25] Pettersson U, Jacobson S. Tribological texturing of steel surfaces with a novel diamond embossing tool technique. Tribol Int 2006;39:695–700.

[26] Cannon AH, King WP. Microstructured metal molds fabricated via investment casting. J Micromechanics Microengineering 2010;20:25025.

[27] Cannon AH, King WP. Casting metal microstructures from a flexible and reusable mold. J Micromechanics Microengineering 2009;19:95016.

[28] Wang X, Kato K, Adachi K. The lubrication effect of micro-pits on parallel sliding faces of SiC in water. Tribol Trans 2002;45:294–301.

[29] Wang X, Kato K. Improving the anti-seizure ability of SiC seal in water with RIE texturing. Tribol Lett 2003;14:275–80.

[30] Wang X, Kato K, Adachi K, Aizawa K. Loads carrying capacity map for the surface texture design of SiC thrust bearing sliding in water. Tribol Int 2003;36:189–97.

[31] Moshkovith A, Perfiliev V, Gindin D, Parkansky N, Boxman R, Rapoport L. Surface texturing using pulsed air arc treatment. Wear 2007;263:1467–9.

[32] Nanbu T, Ren N, Yasuda Y, Zhu D, Wang QJ. Micro-textures in concentrated conformal-contact lubrication: effects of texture bottom shape and surface relative motion. Tribol Lett 2008;29:241–52.

[33] Etsion I. Improving tribological performance of mechanical components by laser

surface texturing. Tribol Lett 2004;17:733–7.

[34] Arghir M, Roucou N, Helene M, Frene J. Theoretical analysis of the incompressible laminar flow in a macro-roughness cell. J Trib 2003;125:309–18.

[35] Sahlin F, Glavatskih SB, Almqvist T rn, Larsson R. Two-dimensional CFD-analysis of micro-patterned surfaces in hydrodynamic lubrication. J Trib 2005;127:96–102.

[36] Liem N Van, Zhenpeng W, Renqiang J. Effect of shape/size and distribution of microgeometries of textures on tribo-performance of crankpin bearing. Proc Inst Mech Eng Part J J Eng Tribol 2022;236:421–33.

[37] Mishra SP, Polycarpou AA. Tribological studies of unpolished laser surface textures under starved lubrication conditions for use in air-conditioning and refrigeration compressors. Tribol Int 2011;44:1890–901.

[38] Nakano M, Korenaga A, Korenaga A, Miyake K, Murakami T, Ando Y, et al. Applying micro-texture to cast iron surfaces to reduce the friction coefficient under lubricated conditions. Tribol Lett 2007;28:131–7.

[39] Yu H, Wang X, Zhou F. Geometric shape effects of surface texture on the generation of hydrodynamic pressure between conformal contacting surfaces. Tribol Lett 2010;37:123–30.

[40] Ryk G, Etsion I. Testing piston rings with partial laser surface texturing for friction reduction. Wear 2006;261:792–6.

[41] Ferreira RTS, Lilie DEB. Evaluation of the leakage through the clearance between piston and cylinder in hermetic compressors. International Compressor Engineering Conference 1984;424.

[42] Pandeya PN, Soedel W. Rolling piston type rotary compressors with special attention to friction and leakage. International Compressor Engineering Conference 1978;268.

[43] Silva LR, Deschamps CJ. Modeling of gas leakage through compressor valves. Int J Refrig 2015;53:195–205.

[44] Yuan X, Chen Z, Fan Z. Calculating model and experimental investigation of gas leakage. International Compressor Engineering Conference 1992;919.

[45] Alves MVC, Barbosa Jr JR, Prata AT, Ribas Jr FA. Fluid flow in a screw pump oil supply system for reciprocating compressors. Int J Refrig 2011;34:74–83.

[46] Cho H, Yoo B-K, Kim Y. CFD Simulation on the Oil Pumping System of a Variable Speed Scroll Compressor. Internatinoal Compressor Engineering Conference 2002;1605.

[47] Kerpicci H, Onbasioglu S, Yagci A, Oguz E. Numerical investigation of oil flow in a hermetic reciprocating compressor. International Compressor Engineering Conference 2010;2019.

[48] Posch S, Hopfgartner J, Berger E, Zuber B, Schöllauf P, Almbauer R. Numerical analysis of a hermetic reciprocating compressor oil pump system. Int J Refrig 2018;85:135–43.

[49] Kerpicci H, Yagci A, Onbasioglu SU. Investigation of oil flow in a hermetic reciprocating compressor. Int J Refrig 2013;36:215–21.

[50] Kim HJ, Lee TJ, Kim KH, Bae YJ. Numerical simulation of oil supply system of reciprocating compressor for household refrigerators. International Compressor Engineering Conference 2002;1533.

[51] Lückmann AJ, Alves MVC, Barbosa Jr JR. Analysis of oil pumping in a reciprocating compressor. Appl Therm Eng 2009;29:3118–23.

[52] Posch S, Hopfgartner J, Heimel M, Berger E, Almbauer R, Schöllauf P. A Numerical Investigation of the Oil Pump Suction Behaviour in a Hermetic Reciprocating Compressor. International Compressor Engineering Conference 2016;2427.

[53] Ozsipahi M, Cadirci S, Gunes H, Sarioglu K, Kerpicci H. A numerical study on the lubrication system for a hermetic reciprocating compressor used in household refrigerators. Int J Refrig 2014;48:210–20.

https://doi.org/https://doi.org/10.1016/j.ijrefrig.2014.09.002.

[54] Ozsipahi M, Kose HA, Cadirci S, Kerpicci H, Gunes H. Experimental and numerical investigation of lubrication system for reciprocating compressor. Int J Refrig 2019;108:224–33.

[55] Prata AT, Barbosa Jr JR. Role of the thermodynamics, heat transfer, and fluid mechanics of lubricant oil in hermetic reciprocating compressors. Heat Transf Eng 2009;30:533–48.

[56] Zhu Y, He G, Sun W, Shimoji M, Chen X. Investigation on the characteristics of oil supply system for a hermetic variable speed rotary compressor. Int J Refrig 2020;118:150–60.

[57] Posch S, Hopfgartner J, Berger E, Zuber B, Almbauer R, Schöllauf P. Determination of the oil distribution in a hermetic compressor using numerical simulation. Conf. Ser. Mater. Sci. Engineering 2017; 232:12009.

[58] Posch S, Berger E, Heimel M, Hopfgartner J, Almbauer R, Schöllauf P. Fluid Flow in the Oil Pumping System of a Hermetic Compressor. IOP Conf. Ser. Mater. Sci. Eng., vol. 90, IOP Publishing; 2015, p. 12028.

[59] Alves MVC, Barbosa Jr JR, Prata AT. Analytical and CFD modeling of the fluid flow in an eccentric-tube centrifugal oil pump for hermetic compressors. Int J Refrig 2013;36:1905–15.

[60] Wu W, Li J, Lu L, Feng Q. Analysis of oil pumping in the hermetic reciprocating compressor for household refrigerators. International Compressor Engineering Conference 2010; 1957.

[61] Ozsipahi M, Cadirci S, Gunes H, Sarioglu K. A Comparison Of An Analytical And Numerical Flow Model For The Lubrication System Of A Variable Speed Hermetic Compressor. Journal Therm Sci Technol 2016;36.

[62] Ye Z, Chu C, Zhang D, Ma S, Guo J, Cheng Y, et al. Study on 3D-Direct Ink Writing based on adding silica submicron-particles to improve the rheological properties of alumina ceramic ink. Mater Today Commun 2021;28:102534.

[63] Wang R-H, Wang X-Q, Song J-G, Xu M-H, Li Y-Q, Liu J-Q, et al. Effect of Sintering Temperature on Properties of Al 2 O 3/Al Cermets n.d. Material Science and Engineering 2017; 494-499.

[64] Hammel EC, Ighodaro O-R, Okoli OI. Processing and properties of advanced porous ceramics: An application based review. Ceram Int 2014;40:15351–70.

[65] Besisa DHA, Ewais EMM. Advances in functionally graded ceramics—Processing, sintering properties and applications. Adv Funct Graded Mater Struct 2016:1.

[66] Qi YE, Zhang YS, Fang Y, Hu LT. Design and preparation of high-performance alumina functional graded self-lubricated ceramic composites. Compos Part B Eng 2013;47:145–9.

[67] Rane K, Petrò S, Strano M. Evolution of porosity and geometrical quality through the ceramic extrusion additive manufacturing process stages. Addit Manuf 2020;32:101038.

[68] Refugio Garcia E, Osorio Ramos J, Rocha-Rangel E, Perez de la Fuente A, MIRANDA HERNANDEZ JG. Ceramic Matrix Composites Reinforced with Metal Nanoparticles n.d. Journal of Welfenia 2015;22:6.

[69] Cong HT, Yang ZQ, He LL, Lu K. Strengthen mechanism of Al2O3/Al nano-composite. Acta Metall Sin 2003;39:320–4.

[70] Peng Y, Wang H, Zhao C, Hu H, Liu X, Song X. Nanocrystalline WC-Co composite with ultrahigh hardness and toughness. Compos Part B Eng 2020;197:108161.

[71] Song JG, Liu Y, He L, Li JS, Chen W, Yang Y, et al. Influence of Ball Milling Process on the Pinned Effect of Al2O3/Al Cermet Composite Powder. Key Eng. Mater., vol. 777, Trans Tech Publ; 2018, p. 80–4.

[72] Min KH, Oh S-T, Do Kim Y, Moon I-H. Processing and fracture toughness of nano-sized Cu-dispersed Al2O3 composites. J Alloys Compd 2003;352:163–7.

[73] Pu B, Zhang X, Chen X, Lin X, Zhao D, Shi C, et al. Exceptional mechanical

properties of aluminum matrix composites with heterogeneous structure induced by in-situ graphene nanosheet-Cu hybrids. Compos Part B Eng 2022;234:109731.

[74] Choi S, Kim J. Thermal conductivity of epoxy composites with a binary-particle system of aluminum oxide and aluminum nitride fillers. Compos Part B Eng 2013;51:140–7.

[75] Nawa M, Sekino T, Niihara K. Fabrication and mechanical behaviour of Al 2 O 3/Mo nanocomposites. J Mater Sci 1994;29:3185–92.

[76] Lieberthal M, Kaplan WD. Processing and properties of Al2O3 nanocomposites reinforced with sub-micron Ni and NiAl2O4. Mater Sci Eng A 2001;302:83–91.

[77] Tuan W-H, Brook RJ. The toughening of alumina with nickel inclusions. J Eur Ceram Soc 1990;6:31–7.

[78] Sun X, Yeomans J. Optimization of a Ductile-Particle-Toughened Ceramic. J Am Ceram Soc 1996;79:2705–17.

[79] Wan H, Leung N, Jargalsaikhan U, Ho E, Wang C, Liu Q, et al. Fabrication and characterisation of alumina/aluminium composite materials with a nacre-like micro-layered architecture. Mater Des 2022;223:111190.

[80] Sardar S, Karmakar SK, Das D. Microstructure and tribological performance of alumina–aluminum matrix composites manufactured by enhanced stir casting method. J Tribol 2019;141.

[81] Vilardell AM, Cinca N, Tarrés E, Kobashi M. Iron aluminides as an alternative binder for cemented carbides: A review and perspective towards additive manufacturing. Mater Today Commun 2022;31:103335.

[82] Shi S, Cho S, Goto T, Sekino T. The effects of sintering temperature on mechanical and electrical properties of Al2O3/Ti composites. Mater Today Commun 2020;25:101522.

[83] Feng H, Zhu P, Guo A, Cheng Z, Zhao X, Gao D. Assessment of the mechanical properties and water stability of nano-Al2O3 modified high ductility magnesium potassium phosphate cement-based composites. Mater Today Commun

2022;30:103179.

[84] Lu H, Sun H, Chen C, Zhang R, Yang D, Hu X. Coating Cu nano-sized particles on Al2O3 powders by a wet-chemical method and its mechanical properties after hot press sintering. Mater Sci Eng A 2006;426:181–6.

[85] Sekino T, Niihara K. Fabrication and mechanical properties of fine-tungsten-dispersed alumina-based composites. J Mater Sci 1997;32:3943–9.

[86] Guichard JL, Tillement O, Mocellin A. Preparation and characterization of alumina–iron cermets by hot-pressing of nanocomposite powders. J Mater Sci 1997;32:4513–21.

[87] Oh S-T, Sekino T, Niihara K. Fabrication and mechanical properties of 5 vol% copper dispersed alumina nanocomposite. J Eur Ceram Soc 1998;18:31–7.

[88] Tuan W-H, Wu HH, Yang TJ. The preparation of AI 2 O 3/Ni composites by a powder coating technique. J Mater Sci 1995;30:855–9.

[89] Lu H, Hu J, Chen C, Sun H, Hu X, Yang D. Characterization of Al2O3–Al nano-composite powder prepared by a wet chemical method. Ceram Int 2005;31:481–5.

[90] Guichard JL, Tillement O, Mocellin A. Alumina-chromium cermets by hot-pressing of nanocomposite powders. J Eur Ceram Soc 1998;18:1743–52.

[91] Ji Y, Yeomans JA. Processing and mechanical properties of Al2O3–5 vol.% Cr nanocomposites. J Eur Ceram Soc 2002;22:1927–36.

[92] Dastanpoor E, Enayati MH, Karimzadeh F. Synthesis of Cu–Zr–Al/Al2O3 amorphous nanocomposite by mechanical alloying. Adv Powder Technol 2014;25:519–23.

[93] Doel TJA, Bowen P. Tensile properties of particulate-reinforced metal matrix composites. Compos Part A Appl Sci Manuf 1996;27:655–65.

[94] Young ML, Rao R, Almer JD, Haeffner DR, Lewis JA, Dunand DC. Load partitioning in Al2O3–Al composites with three-dimensional periodic architecture. Acta Mater 2009;57:2362–75.

[95] Skirl S, Hoffman M, Bowman K, Wiederhorn S, Rödel J. Thermal expansion

behavior and macrostrain of Al2O3/Al composites with interpenetrating networks. Acta Mater 1998;46:2493–9.

[96] Zhao N, Nash P, Yang X. The effect of mechanical alloying on SiC distribution and the properties of 6061 aluminum composite. J Mater Process Technol 2005;170:586–92.

[97] Suryanarayana C. Synthesis of nanocomposites by mechanical alloying. J Alloys Compd 2011;509:S229–34.

[98] Suryanarayana C. Recent developments in mechanical alloying. Rev Adv Mater Sci 2008;18:203–11.

[99] Yoo J, Cima MJ, Khanuja S, EM S. Structural ceramic components by 3D printing. 1993 Int. Solid Free. Fabr. Symp., 1993.

[100] Shahzad A, Lazoglu I. Direct ink writing (DIW) of structural and functional ceramics: Recent achievements and future challenges. Compos Part B Eng 2021;225:109249.

[101] Entezari A, Liu NC, Roohani I, Zhang Z, Chen J, Sarrafpour B, et al. On design for additive manufacturing (DAM) parameter and its effects on biomechanical properties of 3D printed ceramic scaffolds. Mater Today Commun 2020;23:101065.

[102] Qu H. Additive manufacturing for bone tissue engineering scaffolds. Mater Today Commun 2020;24:101024.

[103] Lewis JA, Smay JE, Stuecker J, Cesarano J. Direct ink writing of three-dimensional ceramic structures. J Am Ceram Soc 2006;89:3599–609.

[104] Chen Z, Li Z, Li J, Liu C, Lao C, Fu Y, et al. 3D printing of ceramics: A review. J Eur Ceram Soc 2019;39:661–87.

[105] Mamatha S, Biswas P, Ramavath P, Das D, Johnson R. 3D printing of complex shaped alumina parts. Ceram Int 2018;44:19278–81.

[106] Chen F, Liu K, Sun H, Shui Z, Liu C, Chen J, et al. Fabrication of complicated silicon carbide ceramic components using combined 3D printing with gelcasting.

CeramInt2018;44:254–60.

[107] Xu C, Quinn B, Lebel LL, Therriault D, L'Espérance G. Multi-material direct ink writing (DIW) for complex 3D metallic structures with removable supports. ACS Appl Mater Interfaces 2019;11:8499–506.

[108] Tuttle BA, Smay JE, Cesarano J, Voigt JA, Scofield TW, Olson WR, et al. Robocast Pb (Zr0. 95Ti0. 05) O3 ceramic monoliths and composites. J Am Ceram Soc 2001;84:872–4.

[109] Feilden E, Blanca EG-T, Giuliani F, Saiz E, Vandeperre L. Robocasting of structural ceramic parts with hydrogel inks. J Eur Ceram Soc 2016;36:2525–33.

[110] Cesarano J, Segalman R, Calvert P. Robocasting Provides Mouldless Fabrication From Slurry Deposition. Ceram Ind 1998;148:94–6.

[111] Hartmann K, Krishnan R, Merz R, Neplotnik G, Prinz FB, Schultz L, et al. Robot-assisted shape deposition manufacturing. Proc. 1994 IEEE Int. Conf. 2890–5.

[112] Peng E, Wei X, Garbe U, Yu D, Edouard B, Liu A, et al. Robocasting of dense yttria-stabilized zirconia structures. J Mater Sci 2018;53:247–73.

[113] Schlordt T, Schwanke S, Keppner F, Fey T, Travitzky N, Greil P. Robocasting of alumina hollow filament lattice structures. J Eur Ceram Soc 2013;33:3243–8.

[114] Travitzky N, Bonet A, Dermeik B, Fey T, Filbert-Demut I, Schlier L, et al. Additive manufacturing of ceramic-based materials. Adv Eng Mater 2014;16:729–54.

[115] Chandrasekaran S, Lu R, Landingham R, Cahill JT, Thornley L, Du Frane W, et al. Additive manufacturing of graded B4C-Al cermets with complex shapes. Mater Des 2020;188:108516.

[116] Li W, Armani A, McMillen D, Leu M, Hilmas G, Watts J. Additive manufacturing of zirconia parts with organic sacrificial supports. Int J Appl Ceram Technol 2020;17:1544-1553.

[117] Lu R, Chandrasekaran S, Du Frane WL, Landingham RL, Worsley MA, Kuntz JD. Complex shaped boron carbides from negative additive manufacturing. Mater Des

2018;148:8–16.

[118] Detsch R, Uhl F, Deisinger U, Ziegler G. 3D-Cultivation of bone marrow stromal cells on hydroxyapatite scaffolds fabricated by dispense-plotting and negative mould technique. J Mater Sci Mater Med 2008;19:1491–6.

[119] Tang W, Yan L, Li K, Juan Y, Fu C, Zhang J. A comparison study on aluminum-water reaction with different catalysts. Mater Today Commun 2022;31:103517.

[120] Zheng X, Xu K, Wang Y, Wang Q. Hydrogen inhibition method for preventing hydrogen explosion accident in wet dust removal systems. Int J Hydrogen Energy 2019;44:17195–201.

[121] Khaled B, Abdelbaki B. Rheological and electrokinetic properties of carboxymethylcellulose-water dispersions in the presence of salts. Int J Phys Sci 2012;7:1790–8.